ORIGINAL PAPER

Productivity Decline Mechanisms in Gravel Packed Perforations

Andreas Nicolas Berntsen[1] · Euripides Papamichos[1] · Xiyang Xie[1] · Gang Li[2] · Ziheng Yao[3]

Abstract

In a cased hole gravel pack completion, perforations are packed with proppant to both mechanically support the perforation cavity, and to filter any produced sand before it reaches the surface. Poor perforation packing sometimes occurs in which the perforation is partially or completely unsupported, leading to earlier productivity reduction than in cases of good packing. We investigated productivity reduction and the associated mechanisms in a series of hollow cylinder experiments on outcrop and field cores with varying proppant packing. Packed perforations maintained significantly higher productivity than unsupported perforations by preventing macroscopic shear failure around the cavity and erosion due to sand production. Partial packing may in some instances maintain productivity almost as well as complete packing, but this likely depends on perforation orientation. Compaction tests and numerical simulations suggest that compaction failure is unlikely at the cavity wall in the current experiments, and that proppant-formation interface damage or proppant filtering of produced sand are more probable explanations for the productivity reduction seen in packed perforations.

Highlights

- Hollow cylinder flow experiments show how perforation productivity depends on proppant packing.
- Partial packing may be very effective in vertically oriented perforations.
- Detailed pressure measurements reveal where along the flow path pressure drops increase.
- Proppant-formation interface damage or proppant filtering are probable causes of the productivity decline seen in packed perforations.

Abbreviations

ϕ (–)	Porosity
ϕ_0 (–)	Reference porosity
k (m²)	Permeability
k_0 (m²)	Reference permeability
k_i ($i = 1, 2, 3$) (m²)	Fitting parameters in permeability equation
J_2 (Pa)	Second stress invariant
K_0 (–)	The ratio of radial to axial stress in compaction tests
L (–)	Pressure cap ellipse center
μ (Pa·s)	Dynamic viscosity
p' (Pa)	Effective mean stress
p_c (Pa)	Hydrostatic grain crushing stress
p_{ext} (Pa)	Average pressure at the external specimen boundary
$p_{ext-btm}$ (Pa)	Pressure at the bottom of the external specimen boundary
$p_{ext-top}$ (Pa)	Pressure at the top of the external specimen boundary
p_{HC} (Pa)	Hollow cylinder mean stress
P_{Neq} (–)	Equivalent mean stress ratio
p_{pack} (Pa)	Pressure in the proppant pack in the casing perforation
$p_{perf-btm}$ (Pa)	Pressure in the bottom of the perforation
$p_{perf-top}$ (Pa)	Pressure in the top of the perforation

✉ Andreas Nicolas Berntsen
andreas.berntsen@sintef.no

1 SINTEF Industry, Trondheim, Norway

2 Occidental Petroleum Corporation, Houston, USA

3 Hess Corporation, New York, USA

p_{TRX} (Pa)	Triaxial mean stress
Δp (Pa)	Pressure difference
PI (–)	Productivity index
Q (m³/s)	Volumetric flow rate
r_e (m)	Hollow cylinder external cylinder radius
r_i (m)	Hollow cylinder internal radius
r_y (m)	Hollow cylinder yield radius
R (–)	Pressure cap ellipse major to minor ratio
S_0 (Pa)	Cohesion
σ_c (Pa)	Confining stress
σ_i ($i = 1, 2, 3$) (Pa)	Principal stresses
τ (Pa)	Generalized shear stress
τ_N (–)	Normalized generalized shear stress

1 Introduction

After petroleum wellbores are drilled, they must be prepared for hydrocarbon production by *completing* the well. Well completion may involve merely hydraulically isolating the producing reservoir section while otherwise leaving it open (openhole or barefoot completion), or it may be a more elaborate series of operations placing steel casing, production tubing, valves, etc. The choice of completion depends among others on the formation properties, such as strength and permeability, on the influence of drilling on near-well permeability (formation damage), and on the need for future well operations. Cased and perforated is a common type of completion which entails placing a steel production casing along the reservoir section, cementing the annulus between the casing and the reservoir, and then using directional explosive charges to perforate the casing, cement, and formation at desired intervals. The perforations serve to create the necessary openings in the casing and cement to allow the production of hydrocarbons from the reservoir section, and additionally create highly conductive perforation tunnels in the formation, bypassing the damaged zone (e.g., Bellarby 2009). If there is a risk of sand production (transport of sand grains with the producing hydrocarbons), then sand control equipment may be installed to stop the produced particles from entering the production tubing by filtering, or to prevent the sand from being produced from the formation. In a cased hole gravel pack completion, a screen is set inside the casing, and proppants (natural quartz or synthesized ceramic sand, henceforth used regardless of the actual material) are placed into the screen-casing annulus and perforations. The proppant size is well sorted and selected based on the grain size of the produced sand. It functions as a sand control mechanism by providing mechanical support to the perforation tunnels and trapping produced solids.

Sand production is a combined mechanical and hydrodynamic phenomenon, in which sand grains and debris are transported by the flowing hydrocarbons. Hydrodynamic forces in permeable sands are too low to dislodge cemented grains, even for very weakly consolidated sands (Fjær et al. 2008). The rock must therefore fail mechanically before sand production can commence. In a cylindrical or near-cylindrical cavity, such as a perforation, the tangential (hoop) stress will generally be the largest stress, and the radial stress will be the minimum stress. To produce hydrocarbons, the pressure in the well is reduced to below that of the surrounding formations. This pressure *drawdown* reduces the pore pressure, and thus increases effective stresses in the near-wellbore area. Over time, the pressure in the reservoir is depleted, and the effective stresses increase further. Upon increasing drawdown or, over time, increasing depletion, unsupported perforations may therefore fail in shear, and sand production from the perforation may continue unabated for some time. If, on the other hand, the perforation is filled with proppant, it may support the cavity by increasing the radial stress upon borehole closure and holding in place pieces of material resulting from breakouts/spalling or in the general failure of the cavity.

Early gravel pack operations focused on limiting sand production to the surface, and sometimes left perforations unpacked and vulnerable to collapse and productivity decline that was difficult to remedy. Pre-packing perforations with proppant is now appreciated as important in securing the long-time productivity of the well. Ideally, the entire volume of the perforations is filled with proppant, but poor packing may occur in which case perforations remain partially or completely empty (Fig. 1). This may result from difficult operating conditions, well inclination angles, or proppant flow back from the perforation. Produced sand may accumulate in the perforation and restrict the narrow flow path
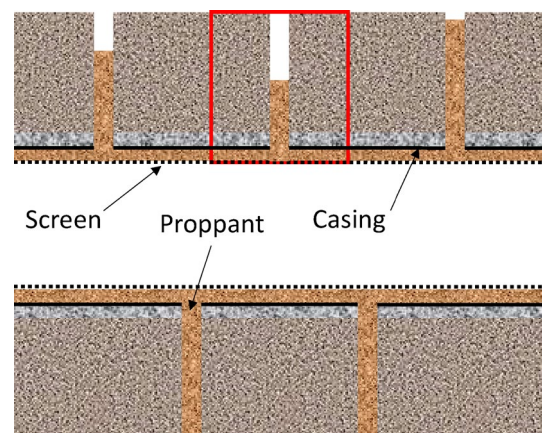

Fig. 1 A cased hole gravel pack completion in a horizontal well section with varying efficiency in the gravel packing of the perforations. The red frame shows the region represented in the experimental setup

through the casing, reducing productivity. However, even good packing efficiency may lead to productivity decline in weak sands since grain crushing may occur around the perforation at large depletions if proppant support is significant. Proppant-formation interactions have been studied, but mostly in the context of propped fractures in low permeability reservoirs. Proppant is necessary to maintain an acceptable fracture width with high permeability, and closure stresses may be large. Here, grain crushing, fines production, and proppant embedment are mechanisms of productivity decline (e.g., Anderson et al. 1989). Crawford et al. (2018) found experimentally that the permeability of the formation-proppant interface was significantly lower than that of the formation under equal stress. Grain cracking within 1–2 mm of the interface was also observed, and both proppant and grain fines were observed to fill the proppant pore space at the interface (Homburg et al. 2018). The closure stresses in fractures are generally higher than those across the proppant-formation interface in a perforation due to the increased cavity tangential stress. Knowledge of the stress states around proppant-packed cavities aid in assessing the probability of various productivity decline mechanisms.

Productivity decline was investigated in a series of experiments on outcrop sandstones and field cores, replicating perforations subjected to a constant drawdown and increasing depletion. The degree of proppant filling was varied to study its effect on productivity decline. Probable productivity decline mechanisms were identified based on differences in pressure loss along the flow path, measurements of perforation yielding, and post-test imaging of the specimen. Triaxial compression tests were done on outcrop sandstone specimens with varying stress ratios to investigate the threshold for grain crushing, compaction, and permeability reduction. The experimental results were used to calibrate a yield criterion with a pressure cap, and to calibrate a model for the permeability reduction with stress. Finite difference modelling was performed to investigate the effect of proppant support on the yielding cavity and to study the stress distribution around the cavity with varying degrees of proppant filling. The experiments and modelling helped us identify the mechanisms of productivity decline resulting from the varying degrees of proppant packing.

2 Experiments

2.1 Perforation Productivity Decline

2.1.1 Experimental Setup

Productivity tests were performed on hollow cylinder specimens with a 20 mm diameter inner hole simulating the perforation. Both outcrop and field core sandstones were used in

testing. The outcrop specimens had 190 mm outer diameter and ca 150 mm height, while field core specimens had ca 100 mm diameter and 100 mm height. For each test, the specimen was placed upright on a steel piston, representing the casing, with a 20 mm center hole. A thin (1 mm) nitrile rubber sheet was placed between the specimen and lower piston to prevent radial fluid flow between the rock and steel, representing the cemented casing-formation annulus. A steel tube of 15 mm inner diameter was connected to the lower piston center hole. The tube was filled with proppant, which was kept in place by a fine metal screen. This represented proppant in the screen-casing annulus. In addition to the cavity pack tests, a reference sand production test was run for each of the outcrop rock types in which the proppant-filled tube was replaced by a bottom assembly with a sand trap and load cell.

Figure 2 shows a schematic of the sand production specimen setup within the sand production ("SBEL") pressure cell. The cylindrical side surface of the specimen is isolated from the confining pressure fluid with an FKM (fluoroelastomer) sleeve which extends upwards and downwards outside the upper and lower pistons, respectively. Isotropic loading is applied at the external surface of the specimen by increasing the confining pressure in the cell. Confining pressure is supplied by a hydraulic power unit and pressure intensifier. The total system is rated at 100 MPa pressure. Radially inward fluid flow in the specimen is achieved by flowing fluid through the top piston (via feedthrough tubing in the cell) and distributing it around the specimen by means of a layer of packed 20/40 mesh proppant between the specimen and the sleeve. The permeability of the distributing proppant layer is
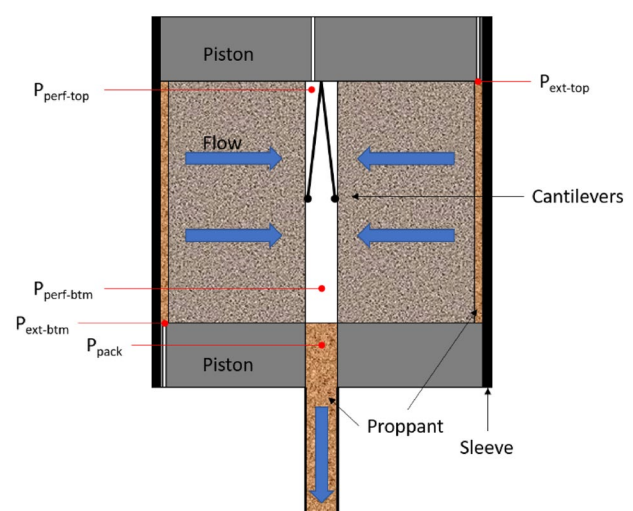

Fig. 2 Schematic representation of the specimen set up with 0% packing in the sand production pressure cell. The positions of the various pore pressure measurements are indicated with red lines

approximately two orders of magnitude higher than that of the rock. This ensures a uniform pressure distribution on the specimen outer boundary and thus a purely radial flow through the specimen at the start of the test. The pore fluid system has a maximum fluid flow rate of 4 L/min and maximum fluid pressure of 40 MPa. It can pump either oil or water. The fluid flow rate and confining pressure are software-controlled in a closed loop using measured values as feedback. For reference sand production tests without proppant in the perforation, a sand trap (Fig. 3) is mounted below the pressure cell for continuous measurement of produced sand.

Pore fluid pressures are measured through ports in the top and bottom pistons at the outer surface of the specimen (diametrically opposite one another), and in the perforation cavity at the specimen top. Additionally, pressures are measured at several points along the flow path from the external specimen surface to the perforation cavity, and along the proppant-filled perforation and steel tube. These measurements allow the calculation of productivity decline along various segments of the flow path, such as across the specimen, along the perforation, etc. Cantilever strain gauges mounted on the top piston measure perforation cavity closure except in the tests with 100% packing efficiency. Figure 2 shows the specimen set-up and the
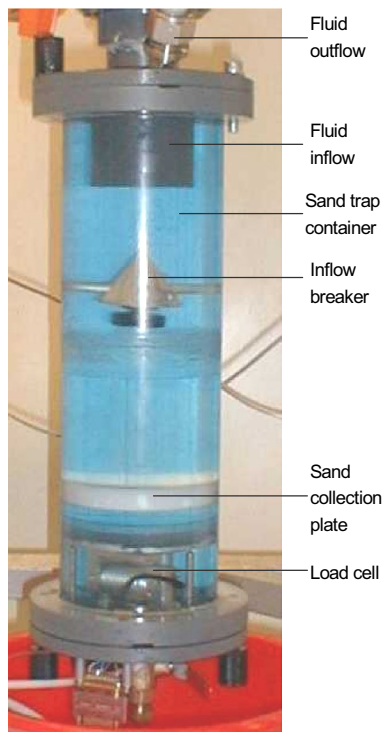

Fig. 3 The bottom assembly of the sand production pressure cell, containing a sand trap with a load cell for continuous measurements of the produced sand

positions of the various pore pressure measurements for a case of 0% packing efficiency.

2.1.2 Material Properties

Two different outcrop sandstones, and one field core, were used to prepare specimens. The two outcrop sandstones represent two of the different failure classes seen in hollow cylinder sand production experiments (Papamichos et al. 2008): Castlegate (Class A) and Saltwash South (Class C). Sandstones are assigned to a class based on their failure patterns in hollow cylinder sand production tests with flow. In addition, the rocks belonging to a given class often exhibit similar characteristics in petrographical analyses and rock mechanical testing. Still, natural rocks are variable and span a continuum of characteristics, so that unambiguous classification may be difficult.

Class A sandstones are characterized by the formation of narrow slits in sand production tests, quickly leading to potential catastrophic sanding. Axial splitting is common in uniaxial compressive tests, while low confinement triaxial testing shows brittle, dilatant behavior. Quartz cementation is common. Castlegate is a medium-weak sandstone with unconfined compressive strength of 16–18 MPa, porosity of 26–27%, and approximately 550 mD permeability. Its unconfined Young's modulus at half peak stress is approximately 3 GPa, while the corresponding Poisson's ratio is ca 0.35. The rock displays water sensitivity, and the listed properties are for dry or oil-saturated rock.

Class C sandstones often show point grain contacts and may have weak and porous cementation. Specimens in uniaxial tests fail by bulging, and in low confinement triaxial tests by compaction. Post-peak behavior is ductile. Sand producing cavities fail uniformly, and erosion by fluid enlarges the original circular shape. Saltwash South is a weak, highly porous, and permeable Class C sandstone. Its unconfined compressive strength is about 1–2 MPa, porosity is 30–31%, and permeability is 2500–3000 mD. Its unconfined Young's modulus at half peak stress is in the range 0.1–0.4 GPa, while the corresponding Poisson's ratio is 0.1–0.2. The rock displays high relative variability in stiffness and strength due to being so weak. It is water sensitive, and the listed properties are for dry or oil-saturated rock.

The field core material generally varied from completely unconsolidated sand to sandy shale. Sand sections were chosen for specimen preparation. Since no reference sand production test was run on the field material, the sandstone class was not evident, but unconsolidated or weakly consolidated field cores often exhibit the characteristics of class C sandstones, with relatively uniform failure and sand production around the perforation.

2.1.3 Specimen Preparation

The outcrop sandstone specimens were drilled from larger blocks of material using a hollow core diamond drill bit with pressured air for bit cooling and cleaning. The center hole thus represented a clean perforation, likely representative of underbalanced perforation, where formation fluids flow into the perforation and clean out debris. The specimens were cut to appropriate lengths (12–15 cm depending on block size and material availability), and their end surfaces were polished to parallelism and flatness within 0.01 mm. They were oven-dried at 80 °C until no further weight loss was observed, weighed, their dimensions measured, and saturated with kerosene in a vacuum desiccator. Total and connected porosity were calculated based on bulk volume, dry and saturated weights, and the assumption that the density of the solid is that of quartz (2650 kg/m^3).

Field core material was supplied in approximately 120 mm diameter, 90 cm long sections in aluminum liners which were slabbed such that approximately 2/3 of the cross-section remained. Based on visual observations and handling of the material, it varied from completely unconsolidated sand to shale that was not suitable for the current experimental program. To obtain usable specimens of the desired size, hollow cylinder specimens were manufactured by joining two halves. Three regions each of 25 cm in length were identified in two adjacent sections of slabbed core (Fig. 4). First, the entire section of the core was frozen to -20 °C. Two 12 cm long sections were then sawed from each region of interest, with the core still inside the liner. Each piece was then submerged in liquid nitrogen, and the core material was separated from the liner using a wire saw combined with heating of the liner. The two halves were then cut to semi-circular cross-sections and joined into a whole cylinder. Steel wire was wrapped around the specimen to hold it together. The center hole was drilled using a 20 mm outer diameter hollow core diamond bit while the specimen was secured in a bracket partially submerged in liquid nitrogen and periodically cooled by pouring liquid nitrogen over the specimen.

The specimen was then mounted on the bottom piston, jacketed with a nitrile sleeve, and proppant was packed between the sleeve and specimen. For the 50% and 100% perforation packing tests, proppant was poured into the center hole to half-height and full height of the specimen, respectively, before the top piston was placed on top. The field cores were mounted while frozen and thawed under a small, initial confining pressure before testing commenced. The interface may lack the packing that characterizes the virgin material, but on the other hand contains smaller grain fragments from the sawing, reducing the permeability of the interface. Combined with the complete lack of interface stiffness due to the unconsolidated nature of the material, it is assumed that the interface between the two original halves does not represent a preferential flow path once an initial confining pressure is applied to the specimen. Freezing represented the only practical method of preparing and mounting unconsolidated specimens. Grain cementation was absent and thus unaffected. Any alteration of the grain packing due to the freeze–thaw cycle would be equally present in all field core specimens, still allowing comparison between them.

2.1.4 Testing Procedure

After the specimen was mounted, the pressure cell was filled with confining oil. A small, initial confining pressure of either 2 MPa for the outcrop specimens, or 0.6 MPa for the field core material was applied to seat the pistons and obtain a reference zero value for all displacement sensors. Paraffin oil was used for flow in all experiments. For the outcrop specimens, radial fluid flow was increased to 3 L/min and
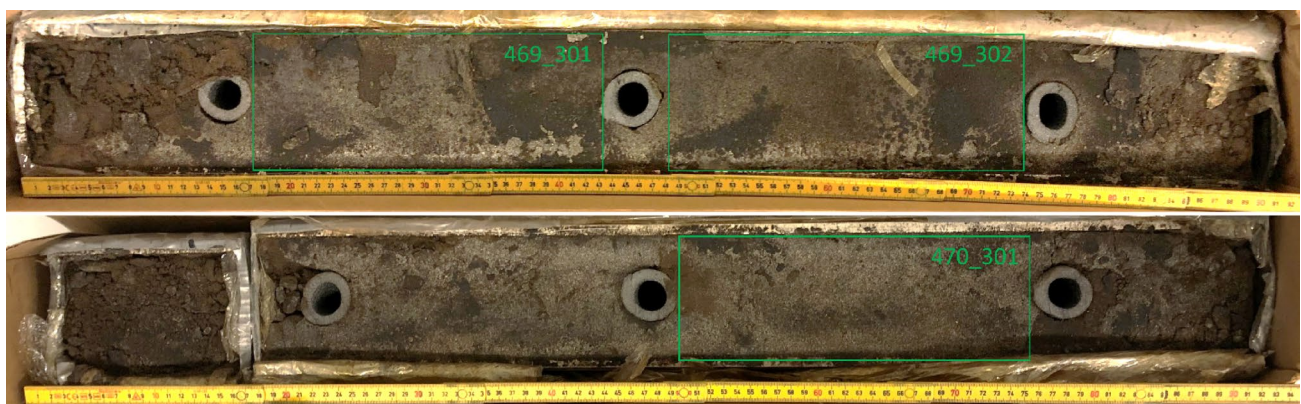

Fig. 4 Two sections of slabbed field core material from which field core hollow cylinder specimens were manufactured. The green rectangles show the lengths used to manufacture each specimen

maintained throughout the test. For the field core material, flow rates were set based on the resulting pressure drop and the need to maintain a lower pore pressure than confining pressure. Details are given in Sect. 4.2. Confining pressure was increased at a rate of 10 MPa/h, and sand production and productivity decline were monitored over the course of the experiment. A reference sand production test was performed for each outcrop sandstone. In these tests, the entire perforation cavity was open, and the produced sand was collected in a sand trap below the specimen. For the reference tests the measured perforation cavity closure and the sand mass were used to identify perforation failure and sanding onset, while for the productivity decline tests, no direct measurement of sand mass was obtained.

For the series of tests on Saltwash South, the proppant-filled tube was rather long at 470 mm, and the two lowermost pressure measurements ($p_{perf-btm}$ and p_{pack}) were 75 mm and 260 mm below the specimen, respectively. This was done to investigate clogging over longer distances. However, it was evident from the tests on Saltwash South that any productivity decline took place in the topmost region of the proppant pack. It was therefore decided to change the positions for the following series of tests on Castlegate. There, the two pressure measurements were taken at 24 mm into the formation, and 12 mm outside the formation as shown in Fig. 2.

2.2 Compaction Tests on Outcrop Sandstone

Triaxial compression tests were performed on Castlegate and Saltwash South specimens to investigate compaction, grain crushing and permeability loss under various stress paths. Three different stress ratios K_0 between the radial and the axial stress were investigated, i.e., $K_0 = 1$, 2/3, and 1/3. The specimens were right cylinders, 38 mm in diameter and 76 mm in length, and prepared similarly as the hollow cylinder specimens (Sect. 2.1).

2.2.1 Experimental Equipment and Setup

Triaxial compaction tests were performed at a conventional triaxial load frame with a confining pressure (radial stress) limit of 100 MPa and axial load capacity of 2.7 MN. The specimen was placed between top and bottom pistons, which included sintered discs for axial permeability measurements and ultrasonic transducers for measurement of ultrasonic travel time through the specimen. Specimen axial deformation was measured using three linear variable differential transformers (LVDTs), while radial deformation was measured with a circumferential chain and displacement gauge. The specimen and top and bottom pistons were jacketed with a 1.4 mm thick Viton rubber sleeve with pressure ports installed at 41 mm axial distance from each other. A differential pressure gauge
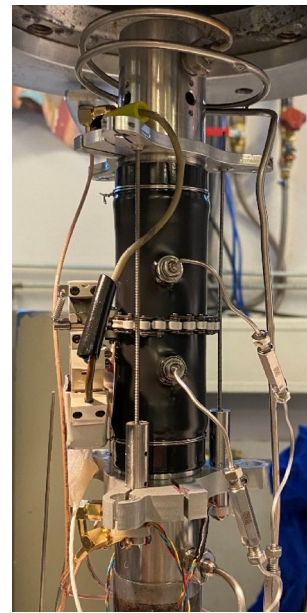

Fig. 5 An instrumented specimen mounted in position for triaxial compression testing. The circumferential chain is placed at mid height of the specimen, while the axial LVDTs are fastened to the top and bottom pistons. Flow ports are visible in the pistons as well as pressure ports in the sleeve

was used to measure the pressure drop across the specimen through the sleeve ports during axial fluid flow. Figure 5 shows an instrumented specimen mounted in position in the load frame.

2.2.2 Testing Procedure

A 0.5 MPa confining pressure was initially introduced to seat the pistons and provide a zero-reference value for displacement sensors. Then the confining pressure was increased to 1 MPa and for tests with $K_0 = 2/3$ and $K_0 = 1/3$, the axial stress was increased to obtain the prescribed stress ratio. Axial flow of kerosene through the specimen at 4 mL/min was introduced at this point, and then for all tests the axial stress and confining pressure were increased proportionally according to the prescribed stress path until specimen failure, or until the maximum confining pressure capacity of the equipment was reached. In all tests, the axial stress was increased at 0.01 MPa/s. Axial flow rate was varied between 1 and 4 mL/min.

Axial stress, confining pressure, axial and radial deformations, ultrasonic pressure and shear waves, and axial differential pore pressure were measured continuously throughout the test. From these measurements, we calculated the axial and radial stresses and strains, the ultrasonic velocities through the specimen, and the axial permeability.

3 Numerical Simulations

Finite difference numerical simulations (FLAC3D, Itasca 2020) were performed on models replicating the geometry and boundary conditions of the perforation productivity decline tests. The simulations aimed to investigate the proppant support around a cavity, and to assess the stress states around supported cavities to evaluate the probability of possible productivity decline mechanisms, e.g., proppant clogging or grain crushing and formation permeability loss. No attempts were made to simulate erosion and sand production.

3.1 Modeling Setup

The hollow cylinder specimen was modelled according to its actual dimensions, a right hollow cylinder of 95 mm outer radius, 10 mm inner radius, and 150 mm height. Axisymmetric conditions were assumed with the axisymmetric axis aligning with the axis of the perforation, giving each point two degrees of freedom (vertical and radial displacement, no rotation). A structured mesh with $3 \times 51 \times 51$ grid points was used, totaling 5000 hexahedral finite volume zones. The mesh was refined towards the perforation such that the radial zone width varied from 0.85 to 3 mm. Three grid points were chosen in the tangential direction as it produced more stable results for the proppant-rock contact. The meshed domain is
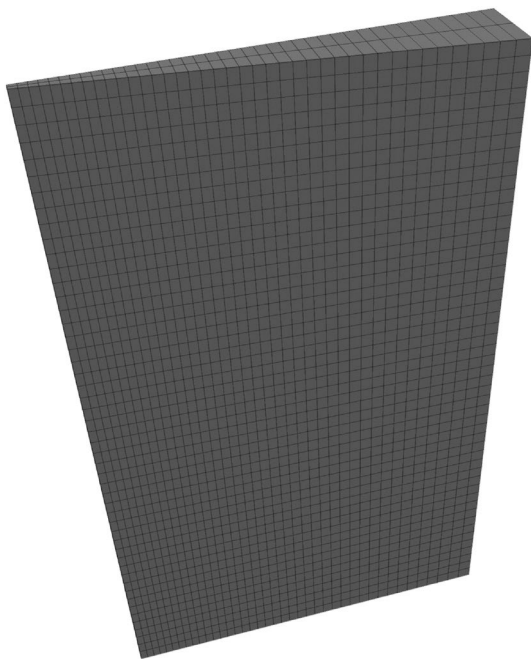
Fig. 6 The meshed domain of the hollow cylinder rock specimen. The left edge is the inner perforation surface, while the right edge is the outer surface of the specimen. The mesh is refined towards the perforation (left)

shown in Fig. 6. The perforation proppant pack for 50% and 100% packing was modelled as an axisymmetric cylinder in contact with the perforation wall. The contact between the proppant and the wall was modeled by a cohesionless and frictionless interface, with only normal forces transferred with the condition of no geometry penetration. Separation was possible if the contact stress became tensile.

In the experiments on outcrops, a constant radial flow rate was applied to the outer surface of the specimen. An equivalent pore pressure boundary condition was applied in the simulation to reduce computational cost relative to a constant flow condition. The pore pressure in the perforation hole was maintained at zero. Confining stress was applied to the outer radial surface of the specimen. For the sake of computational efficiency, a condition of zero vertical displacement was enforced on the top and bottom end faces. This resulted in an axial stress approximately 90% of the radial stress which is close to the isotropic loading used in the tests.

3.2 Material Properties

Castlegate sandstone was modelled as an isotropic, linearly elastic material with a Mohr–Coulomb failure criterion and perfect plasticity. Young's modulus was estimated from axial strain measurements on hollow cylinder loading. The cohesion and internal friction angle were calibrated as 3.4 MPa and 29°, respectively, from a best fit to results from uniaxial and triaxial compression tests at 0–5 MPa confinement. Sandstones often exhibit increasing stiffness with loading and confinement (e.g., Sulem et al. 1999). Since the area of interest is close to the cavity wall, where the minor principal stress (radial) is low, the experimentally derived stiffness at low confinement was chosen. This assumption contributes to a conservative estimate of the elastic radial displacement, which is proportional to the inverse of the elastic modulus. Similarly, a Poisson's ratio of 0.25, deduced from low confinement rather than unconfined compression tests, was employed. Reducing Poisson's ratio for a constant Young's modulus is equivalent to reducing bulk modulus (leading to increased radial displacement at a distance from the perforation) and increasing shear stiffness (leading to reduced radial displacement near the perforation). The net effect is that the radial displacement at the perforation wall is rather insensitive to the choice of Poisson's ratio, with ~ 10% variation in perforation wall displacement for Poisson's ratio between 0.2 and 0.35 under the employed boundary conditions.

Continuum modelling of hollow cylinders with a Mohr–Coulomb yield criterion predicts yielding of an unsupported borehole when the tangential stress reaches the uniaxial compressive strength (UCS) of the material. However, this yielding is not associated with macroscopic failure of the cavity, like breakouts or spalling (e.g. Papamichos

2010; Papamichos et al. 2010). Macroscopic failure is controlled not only by the material UCS but also by the global kinematic boundary conditions (the material may not have the freedom of movement for shear failure to occur) and is affected by the granularity of the material. The latter leads to scale effects for the strength of cavities in granular media (see e.g., Papamichos et al. 2010; Berntsen and Papamichos 2012; Fjær et al. 2017). In the current simulations, the friction angle was chosen equal to the experimentally derived value of 29°, while the cohesion was set to 7.95 MPa so that simulated cavity strain matched the hollow cylinder experimental values. This corresponds to a UCS of 27 MPa which was higher than the value calculated by straight-line fitting of the triaxial compression test results which was 17.3 MPa. The cohesion and friction angle from the triaxial tests in turn slightly overpredicted the measured uniaxial strength of 14.2 MPa, which is quite commonly observed. A better fit with the experimental data would have required a nonlinear Mohr–Coulomb criterion which is avoided for simplicity. An associated plastic flow rule was assumed, where dilation angle equals to friction angle. Peak dilation angles for sandstones can be quite high (30–50 degrees) under low confinement (0–2 MPa), but reduce markedly with both confinement and plastic shear (e.g., Zhao and Cai 2010). This assumption is thus most appropriate for the cases where the perforation is not significantly supported.

The properties of ceramic proppant under high confinement have been studied previously. Han et al. (2015) found the bulk and shear moduli of a pack of 30/50 ceramic proppants to be 10 and 3 GPa, respectively, and that a cohesionless yield criterion with increasing frictional mobilization with plastic strain gave good agreement between simulations and constant mean stress compression experiments. However, the proppant packs in the current experiments are not pre-stressed, and even the proppant in the 100% packed cavity has some vertical freedom of movement due to the shape of the top end cap. For simplicity, the proppant in the current work was modelled as an isotropic, linearly elastic material with a Mohr–Coulomb yield criterion and perfect plasticity. Zero dilation was assumed since the proppant was very loosely packed and not pre-stressed. The friction angle was chosen based on the results from Han et al. (2015), while cohesion was determined by best fitting to match yield patterns seen in post-test CT scans of the specimens, and by the condition that the cohesion be low compared to that of the rock. The properties used in the simulations are summarized in Table 1.

3.3 Simulation Setup

An initial flow condition of 3 L/min was enforced at the outer boundary of the sample to match experiments. After flow had reached stationary conditions, the flow condition

Table 1 Constitutive parameters used in the simulations

Property	Unit	Value
Hollow cylinder rock sample		
Young's modulus	GPa	2.5
Poisson's ratio	–	0.25
Cohesion	MPa	7.95
Friction angle	degrees	29
Dilation angle	degrees	29
Porosity	–	0.278
Permeability	mDarcy	550
Inner diameter	mm	20
Outer diameter	mm	190
Height	mm	150
Proppant		
Young's modulus	GPa	1
Poisson's ratio	–	0.25
Cohesion	MPa	3.8
Friction angle	degrees	33
Dilation angle	degrees	0
Tensile strength	MPa	0.1
Pack height	mm	0/75/150
Rock-proppant interface		
Cohesion	MPa	0
Friction angle	degrees	0
Interface stiffness	GPa	2105
Fluid		
Bulk modulus	GPa	2.25

was exchanged for an equivalent pore pressure boundary condition on the external surface (0.33 MPa) due to the lower computational cost. The pore pressure in the perforation was maintained at zero. Radial stress was then increased at appropriate steps for convergence.

4 Results

4.1 Reference Sand Production Tests

The perforation cavity of the Saltwash South reference specimen indicated failure at approximately 15 MPa as the deviation of the two orthogonal strain measurements (Fig. 7). Strain accelerated with further increase of confining pressure, with a noticeable change of strain rate as measured by both set of calipers at approximately 18–19 MPa. Measurable sand production started at ca. 18.6 MPa (Fig. 8). The apparent permeability k of a straight hollow cylinder under radial flow can be calculated as
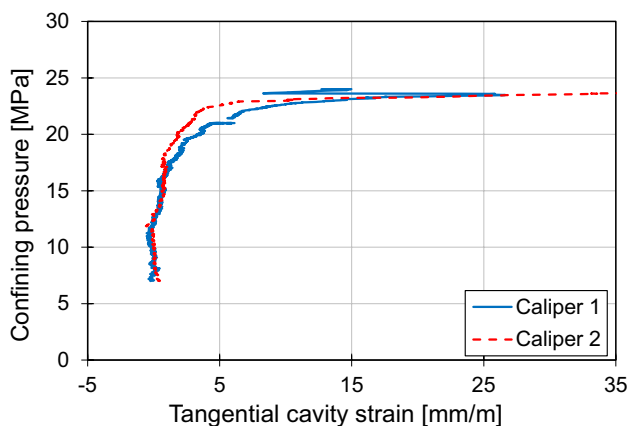
Fig. 7 Tangential cavity strain for Saltwash South sand production reference test. Yielding initiated at approximately 15 MPa
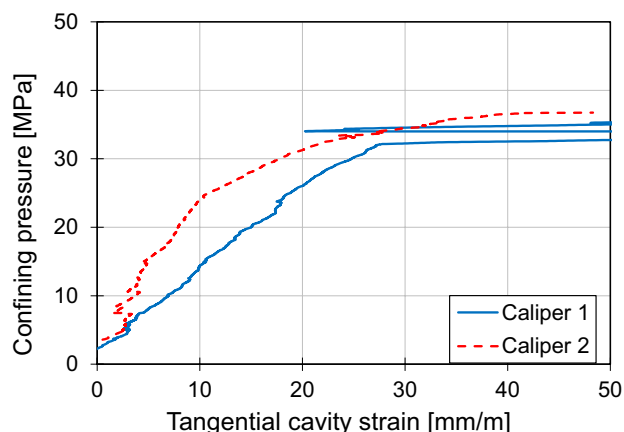

Fig. 9 Tangential cavity strain for the Castlegate reference sand production test
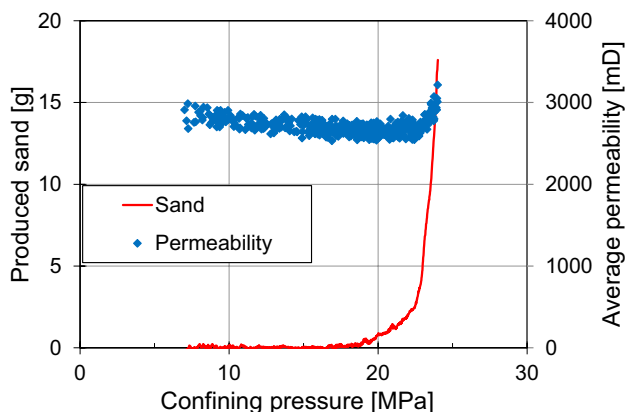

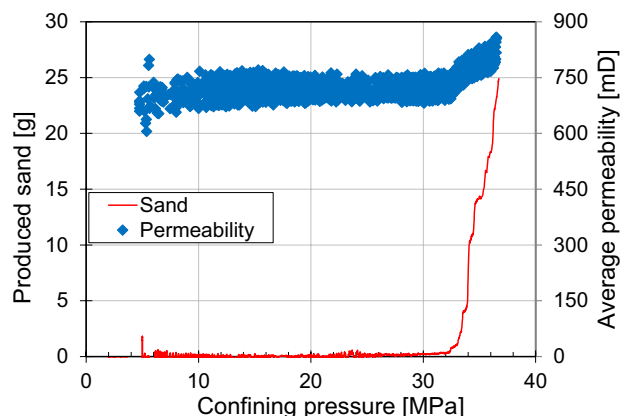**Fig. 8** Measured sand production and calculated apparent permeability for Saltwash South reference sand production test

Fig. 10 Measured sand mass and calculated average specimen permeability for the Castlegate reference sand production test

$$k = Q\mu \frac{\ln\left(\frac{r_e}{r_i}\right)}{\Delta p} \tag{1}$$

where Q is volumetric flow rate, μ is dynamic viscosity, r_e and r_i are external and internal cylinder radii respectively, and Δp is the pressure difference between the inner and outer radii. Flow rate is controlled, while pore pressure is measured at several points during the experiments.

A reduction of permeability over time is observed until approximately 22 MPa. This may be due to compaction of the weak sandstone—although not corroborated by compaction tests under isotropic conditions (Sect. 4.4)—but is likely due to the absence of a nitrile sheet between the specimen and pistons in this test, allowing for larger flow along the interface at lower confining pressure. After 22 MPa, the erosion of the cavity following sand production caused the apparent permeability to increase, since a constant specimen size is assumed in the calculation. Measured sand production

occurred slightly after cavity yielding as expected (Berntsen and Papamichos 2012).

The first indication of cavity yielding for the Castlegate reference sand production test (Fig. 9) came at 22–25 MPa, where especially the strain in direction two (dashed red line) accelerated. Direction one (blue solid line) showed a sharp increase at 32.5 MPa, corresponding to a shear failure breakout. The significant increase in tangential strain coincides with the measurable initiation of sand production seen in Fig. 10. As for the Saltwash South test, cavity erosion resulted in an increase of apparent permeability. Both cavity yielding and sand production were more abrupt in the Castlegate specimen than for Saltwash South, consistent with the erosion patterns observed for these sandstone classes (Papamichos et al. 2008).
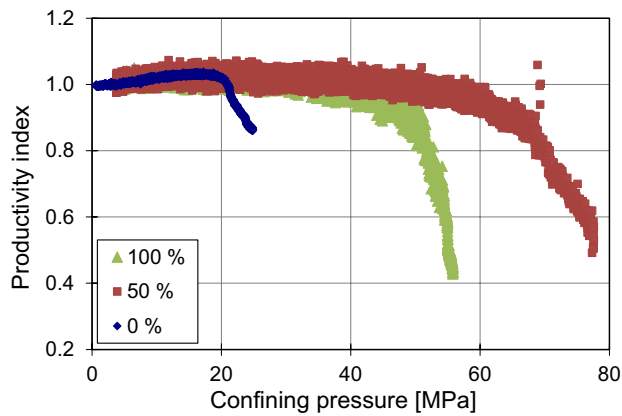
Fig. 11 Productivity decline for Saltwash South specimens with varying degrees of perforation packing
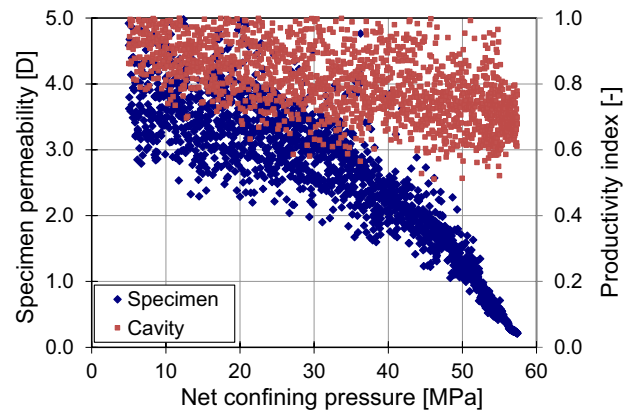

Fig. 12 Calculated average permeability across the specimen (outer proppant layer to center of perforation), and Productivity Index of the packed perforation cavity (from top to bottom) for Saltwash South 100% packed perforation test

4.2 Perforation Productivity Tests

4.2.1 Productivity Tests on Saltwash South

Productivity in the current tests is defined as volumetric flow divided by the pressure difference between two points along the flow path. The total productivity is based on the pressure difference between the outer specimen boundary (p_{ext}) and atmosphere. The productivity index (PI) is the productivity normalized by a reference value early in the experiment. For the productivity decline tests, produced sand was not measured directly, but measurements of the pore pressure at various locations along the flow path indicate sand onset and give insight into the mechanisms of productivity decline for various degrees of packing. Figure 11 plots the productivity index as a function of confining pressure for the three different packing efficiencies in the Saltwash South tests. The 0% pack test shows a marked PI decline starting at 18 MPa, the same confining pressure at which the reference tests started to produce sand (cf. Fig. 8). The perforation in the 0% pack test is completely unsupported and is therefore expected to produce similar sand as the reference test. Any sand that is produced from the 0% pack test collects in the proppant and may potentially clog it at the perforation entrance. This assertion was supported by pressure readings that showed that the upper layer of proppant at the entrance was responsible for the entire PI decline of the system. The PI across the rock specimen increased similarly as the reference test due to cavity erosion.

The 100% packed perforation test was run to a higher confining pressure before PI decline accelerated at approximately 48 MPa. Proppant filled the entire perforation, both supporting the cavity and preventing failed material from being produced. Figure 12 shows that the productivity decline in the completely packed perforation is mainly due to flow resistance radially between the outer rock periphery and the perforation center and not in the proppant along the perforation. The proppant pack provides radial stress support to the cavity wall and leads to a different productivity reduction mechanism. CT scans of the specimens after testing reveal shear bands in the 100% packed perforation only in the topmost region, but not at the center height of the specimen. The test with 50% packing was interestingly run to even higher confining pressure before significant PI decline was observed (Fig. 11). The failure and fracturing of the upper half of the specimen may have provided an increase in specimen PI, while the packed lower half of the perforation ensured a bypass of the clogged upper surface of the proppant. Although the reason is not clear, it is more clearly identified in the case of Castlegate due to additional pressure measurements (cf. Sect. 4.3). Figure 13 shows CT scans of the four Saltwash South specimens after testing. The reference sand production test caused erosion through the entire specimen all the way to the outer surface.

4.2.2 Productivity Tests on Castlegate

The test setup was improved based on experience from the series on Saltwash South. The pore pressure probes along the flow path were moved so that more measurements were obtained in and close to the perforation (Fig. 2). Sensitive differential pressure gauges were installed to capture small changes in PI in the different regions. Additionally, external axial deformation measurements were included. Cavity closure in the Castlegate 0% packing test was, after an initial period of non-linearity until 10–12 MPa, quite linear from 12 to 22 MPa, albeit with some uneven increases in caliper 1 (Fig. 14). It is not clear at what stress level the perforation starts to yield, but it seems to be at 21–25 MPa, similarly to the reference test at 22–25 MPa (Fig. 9). This subtle yield
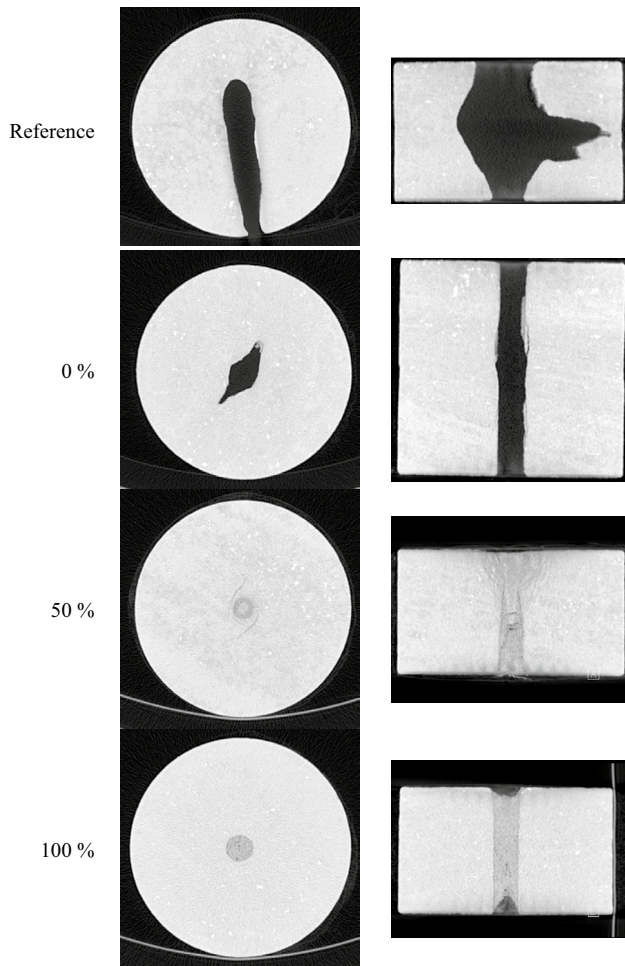
Fig. 13 CT scans of Saltwash South specimens after testing. Left column shows axial center slices; right column shows diametrical slices. From top to bottom: Reference, 0%, 50%, 100% pack
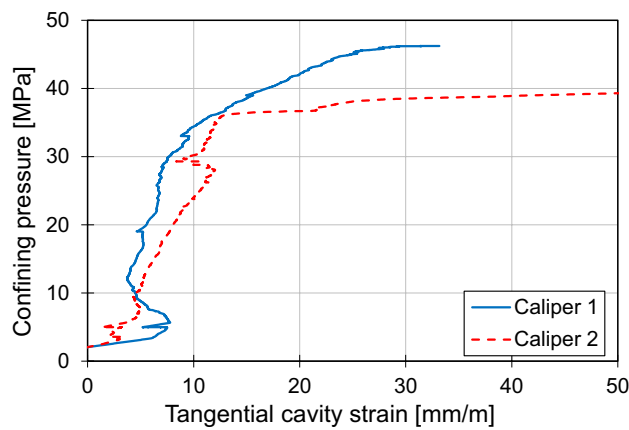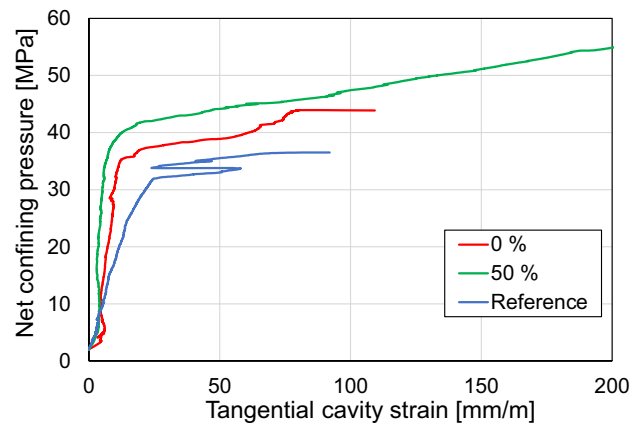

Fig. 15 Tangential cavity strain (average of two orthogonal directions) for each of the Castlegate perforation packing tests

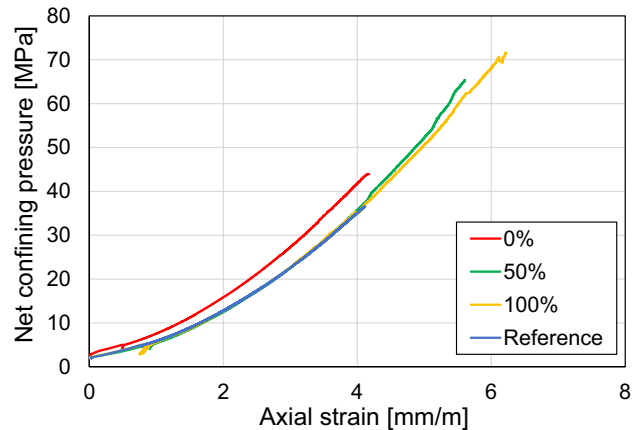Fig. 16 Axial strain for all cavity tests on Castlegate

Fig. 14 Tangential cavity strain in two orthogonal directions for the Castlegate 0% pack test

characteristic is not evident when the two orthogonal strain measurements are averaged as in Fig. 15. The 0% pack test was expected to behave as the reference test but showed less cavity straining for a given level of confining stress. Calculated axial strain from the average of two axial deformation measurements (LVDTs) show very similar behaviour for all specimens (Fig. 16), although the 0% pack at first glance seems slightly stiffer. One of the two LVDTs malfunctioned during this test, and its data were not included in the averaging. This likely explains the apparent discrepancy. The test with 50% packing shows delayed cavity yielding with respect to the unsupported case. Small displacements are noticeable at both 25 MPa and 32 MPa, but consistent increase in strain rate occurs first at 35 MPa. Even though half of the perforation remains unsupported, the packed region may alter the kinematic boundary conditions of the unsupported region, delaying the development of shear breakouts.
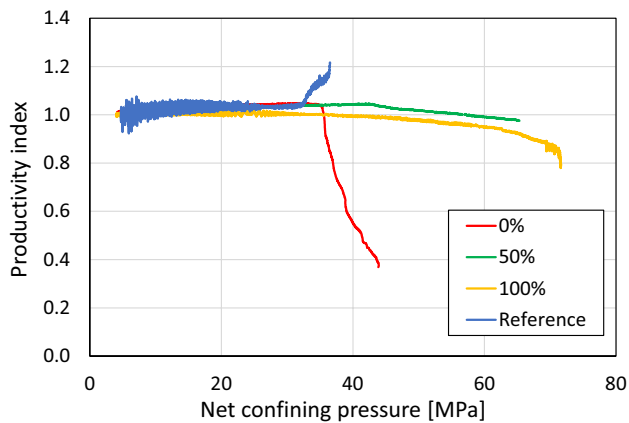
Fig. 17 Productivity index evolution for all cavity tests on Castlegate

Figure 17 plots the PI evolution for all tests on Castlegate. The trend is similar to that of Saltwash South where for the 0% pack test a large PI decline is observed at the sand production stress of the reference test, while for the 50% and 100% pack tests PI decline commences at significantly higher stress. The 50% packed perforation maintains a higher PI than the completely packed perforation throughout the test. The details supporting this are presented in Sec. 4.3 when analyzing data from pressure measurements along the flow path. The 50% pack test was stopped prematurely due to a rupture of the sleeve. For the completely unsupported perforations, the reference test shows an increase in PI due to the removal of material as sand grains are free to move into the wellbore. On the other hand, in the 0% packed test, the produced material causes a significant PI decline because it plugs the gravel pack.

CT scans of the specimens after testing revealed that the unsupported cavities produce sand from slit-like erosion channels that are typically seen in Class A sandstones with one phase flow (Fig. 18). The partially and completely packed perforations did not produce such slits, but rather showed typical shear breakouts in the regions of least support.

4.2.3 Productivity Tests on Unconsolidated Field Core

Figure 19 shows the timeline of the 0% packed field core productivity test. All deformation measurements are with reference to the 0.5 MPa confining pressure at the start of the test. Confining pressure was first increased to 2 MPa. Pore pressure was introduced to the outer surface of the specimen and was maintained for 200 s at 1.5 MPa which is slightly below the confining pressure at 2 MPa, but without any discernible flow through the specimen. Confining pressure was then increased to 5 MPa to prevent the injection pressure from increasing above the confining pressure, and
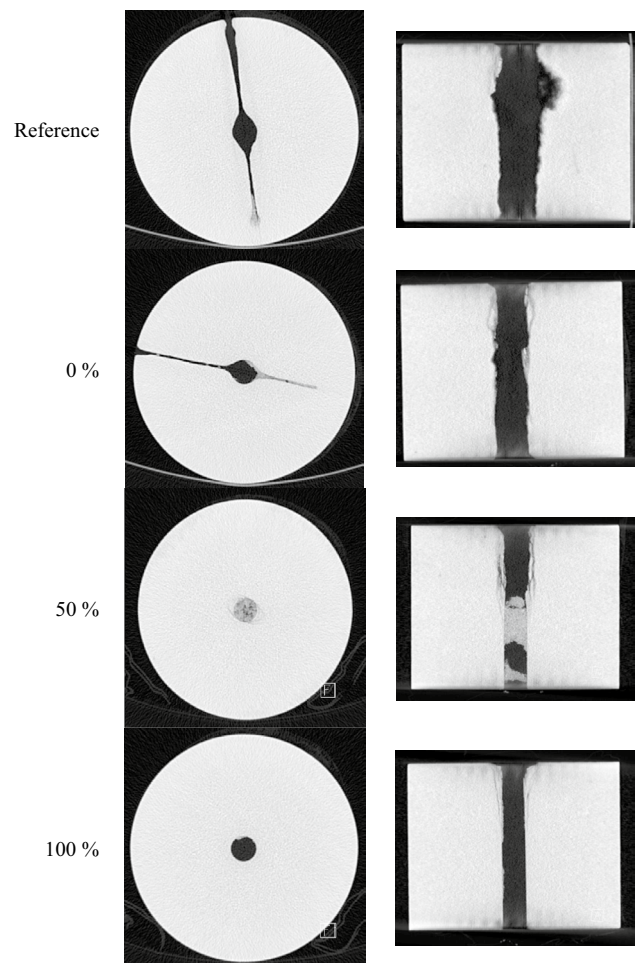
Fig. 18 CT scans of Castlegate specimens after testing. Left column shows axial center slices; right column shows diametrical slices. From top to bottom: Reference, 0%, 50%, 100% pack. The proppant in the 100% pack specimen was removed before CT scanning
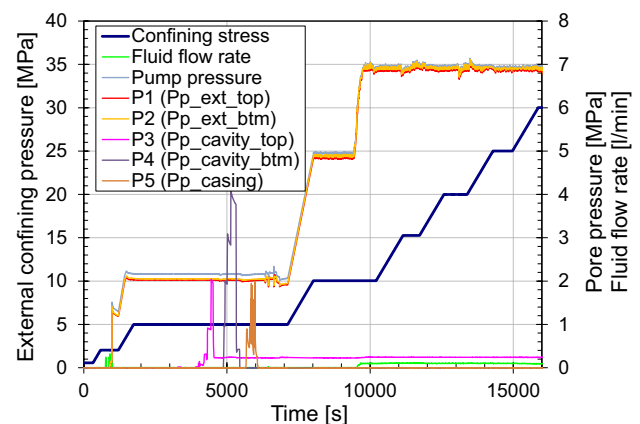

Fig. 19 Timeline of the 0% pack field core productivity test

external pore pressure was increased to 2 MPa and maintained for 2500 s. Two pressure gauges placed diametrically opposite each other ($p_{ext-top}$ and $p_{ext-btm}$ in Fig. 2) both confirmed the external pore pressure, while pressure in the cavity ($p_{cavity-btm}$ and $p_{cavity-top}$) and in the casing perforation (p_{pack}) all showed zero pressure. To investigate the possible mechanisms preventing flow, lamp oil was slowly pumped into the cavity top (through the pressure tubes), and then into the cavity bottom. In both instances, pressure built up locally but did not communicate to the other pressure gauges. Finally, lamp oil was pumped into the casing perforation (p_{pack}) at 1.5 mL/min for 20 min. The pump pressure fluctuated between 0.3 and 2 MPa during injection, while all other pressure measurements were unaffected. The pressure at $p_{cavity-top}$ did not return to zero after local injection was stopped which indicated a possible blockage of the pressure tube.

Confining pressure was increased to 10 MPa, and external pore pressure to 5 MPa, after which oil started to flow through the specimen. External pore pressure was then increased to 7 MPa and maintained for the remainder of the experiment. Absolute productivity increased to 0.015 L/(min·MPa) as the lower viscosity lamp oil replaced the crude oil and thereafter reduced slowly over time to 0.013 L/(min·MPa) as confining pressure was stepwise increased to 30 MPa. Productivity was thus almost unaffected by stress increase after 10 MPa, and data on productivity below 10 MPa confining stress was inconclusive since flow through the specimen was not achieved satisfactorily.

When confining pressure was increased from 0.5 MPa (reference level) to 2 MPa, the tangential cavity strain in the 0% packed test increased to 0.4, i.e., it reduced the perforation diameter by 40% (Fig. 20). Creep is evident at periods of constant confining pressure at 2 MPa and 3 MPa. With unconsolidated material, cavity closure may be underestimated if the cantilevers protrude into the soft material.
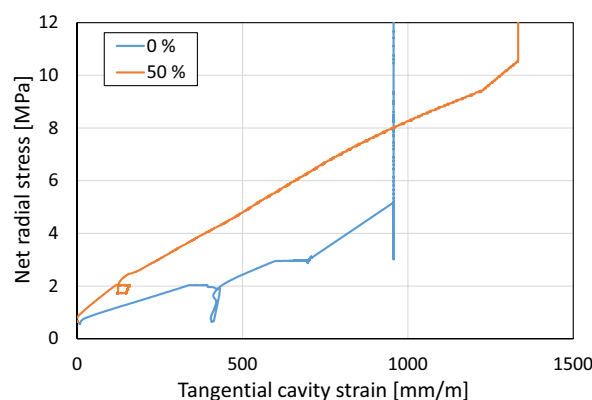

Fig. 21 Net external radial stress versus tangential cavity strain for the partially (50%) supported and unsupported (0%) perforations

Additionally, the cantilever displacement is calibrated in the range ±2.5 mm, so that larger displacements than 8 mm should be treated as indicative rather than quantitative. Further increase of the confining pressure to 5 MPa resulted in large increases in the measured perforation closure and resulted in a measured signal outside the measurement range. Possibly, the perforation at this point was completely closed. Bulk modulus calculated based on axial strain assuming hydrostatic compression was 0.6–0.8 GPa during loading from 0.5 to 2 MPa confining pressure and increased to 3.5–5 GPa during loading from 10 to 30 MPa.

The cavity closure was significantly delayed in the 50% packed perforation as compared with the 0% packed, unsupported perforation, as seen in Fig. 21. In the 50% packed cavity, deformation is measured close to the proppant pack. Axial stiffness increased with the amount of packing. This can be seen in Fig. 22, where axial strain is plotted against net axial pressure, which is confining pressure minus the average fluid pressure exerted on the piston resulting from the radial pore pressure profile.
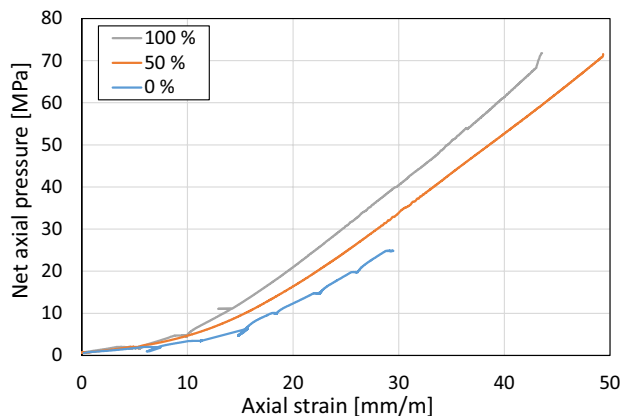

Fig. 20 Axial strain and tangential cavity strain for 0% packed field core test

Fig. 22 Axial strain for the field core productivity tests

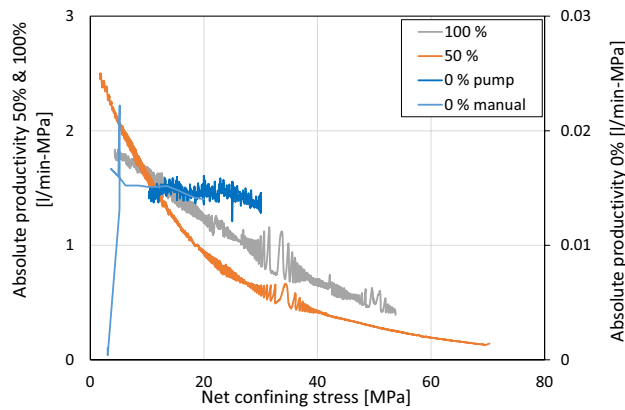Fig. 23 Productivity evolution for tests on field cores. Note that data from the unsupported cavity is plotted on the right hand vertical axis

Fig. 24 PI evolution for Castlegate 0% pack between various measuring points

The evolution of productivity was markedly different for the unsupported (0%) perforation as compared to the partially (50%) or fully (100%) supported perforations. Figure 23 shows the absolute productivity for all three tests. The completely supported perforation maintained higher absolute productivity than the partially supported perforation after surpassing 10 MPa confining pressure. While the supported cavities gradually reduced in productivity from similar initial values, the unsupported perforation had low productivity from the start but reduced thereafter only slightly. Due to the low initial flow rate, manual measurements on produced oil were done in addition to the rate recorded by the flow pump. Fluctuations in productivity can be seen at approximately 32–35 MPa and 50 MPa net confining stress, corresponding to flow pressures of 1 MPa. The fluctuations are due to one of two pressure accumulators, functioning as pulse damping devices, being pressurized at 1 MPa. The fluctuations occur when the pump output pressure corresponds to the pre-load of one of two pulse dampening pressure accumulators connected to the pump output.

4.3 PI Decline Along the Flow Path

4.3.1 Castlegate Outcrop

The measurements from differential pressure gauges placed along the flow path in the Castlegate test series give insights into where along the flow path the PI decline occurs for the tests with different packing efficiencies. Pressure drop is measured, and the PI is calculated for each region. The following regions are defined (cf. Fig. 2): *Specimen* refers to $P_{ext-btm} - P_{perf-btm}$; *cavity* refers to $P_{perf-top} - P_{perf-btm}$; *casing* refers to $P_{perf-btm} - P_{pack}$; *screen* refers to the P_{pack} measured with respect to ambient pressure. The total PI is calculated using the average of the external pore pressures ($P_{ext-top}$ and $P_{ext-btm}$) with respect to ambient.
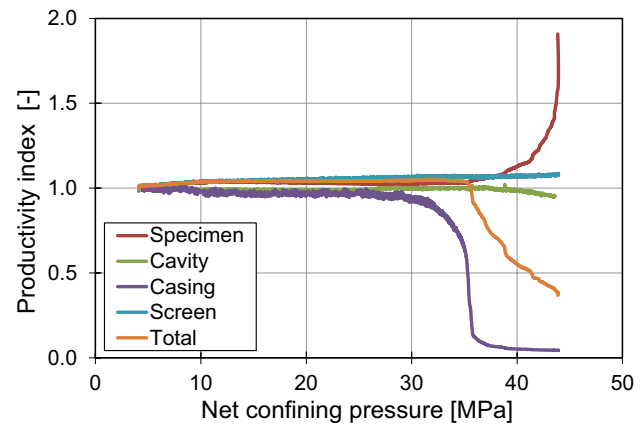
The PI decline in the 0% pack Castlegate test is first observed in the casing region at 27 MPa confining pressure (Fig. 24). Initially, its contribution to total PI decline is slight due to the relatively short flow path it represents (24 mm). The specimen PI increases with erosion, but the net effect is a drastic reduction of PI due to local clogging of the flow path through the casing perforation hole. The cavity PI can be seen to decline towards the end of the test, indicating that the column of produced sand in the perforation had covered the pressure tube 12 mm above the casing-specimen interface. Sand was filtered in the topmost ≤ 24 mm of the proppant bed, as can be seen from the constant *screen* PI during the test.

For the 50% pack test (Fig. 25), PI decline is first observed in the cavity since produced sand now settles on the proppant bed in the middle of the perforation. Decline initiates at 33 MPa confining pressure, which is later than in the completely unsupported perforation. Although PI of the cavity decreases to less than 10% at the end of the test, the
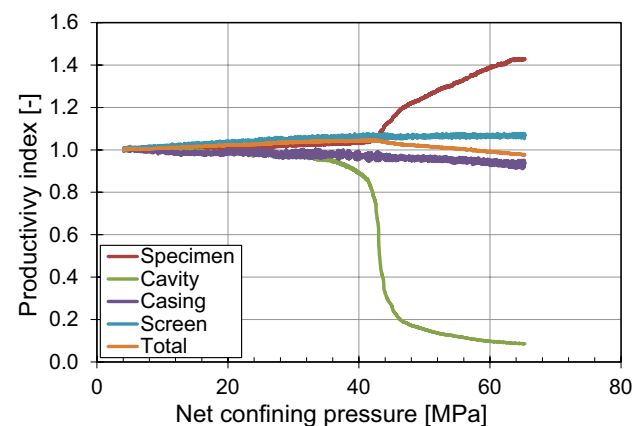

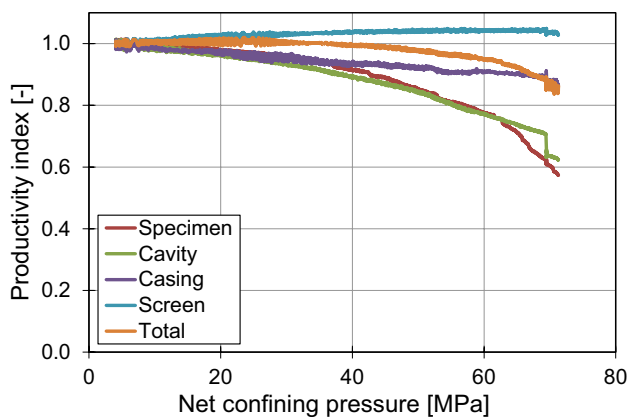Fig. 25 PI evolution for Castlegate 50% pack between various measuring points

Fig. 26 PI evolution for Castlegate 100% pack between various measuring points

impact on total PI is limited since it is not a system bottleneck. The corresponding PI of the casing reaches 1% at the end of the 0% pack test, which has a much more profound impact on total PI. The partially packed perforation supports the cavity, delaying sand onset, and prevents the formation of slit-like erosion paths that have a high sand production potential (Papamichos et al. 2008). Additionally, a high permeability flow path is maintained in the supported region of the cavity, even though the top of the proppant bed may be significantly clogged by sand.

PI reduction happens in all regions except the *screen* for the completely packed perforation (Fig. 26). The highest reductions are seen across the specimen and along the cavity. Note that the *specimen* region also includes the specimen-proppant interface and a certain volume of proppant, since the pressure transducer measures from the center top of the perforation cavity. The *casing* sees only a slight PI reduction, indicating that any sand that is produced does not clog the casing hole.
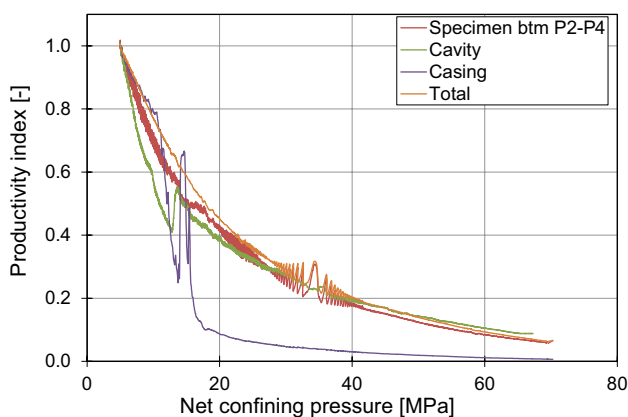
4.3.2 Unconsolidated Field Core

Since no flow was measured through the unsupported (0%) perforation at low confining pressures, no initial productivity was measured. Once flow was established, the resistance to flow was entirely from the radial path across the specimen and into the perforation, while there was no reliable pressure difference measured vertically through the cavity, and no pressure loss measured through the casing or screen. The partially supported perforation (50%) lost productivity with increasing confinement in all parts of the flow path (Fig. 27). Pressure loss radially over the top part of the specimen was very low, while it was high radially over the bottom part of the specimen and vertically through the cavity. This may be an indication that the unsupported, upper region of the cavity had collapsed, creating a high permeability path radially in the top, but significantly reducing productivity vertically along the perforation. At approximately 10 MPa confining pressure, productivity declined quite fast for the *casing* interval, although it did not highly affect the total productivity due to the moderate absolute pressure loss in this interval. The *cavity* productivity was maintained better in the completely supported perforation (Fig. 28), although it did see a significant decrease with loading. Post-test visual inspection of the proppant pack showed remains of crude oil. As for the case of fully supported perforation in Castlegate (Fig. 26), there is significant productivity decline across the specimen. Some data for specimen top and cavity are not plotted, and data for casing is omitted in its entirety, due to pressure measurements in the tests indicating clogging of tubing and thus unreliable results.

4.4 Compaction Tests

Of the six tests that were completed (two rock types, three stress paths), only three obtained grain crushing (Castlegate
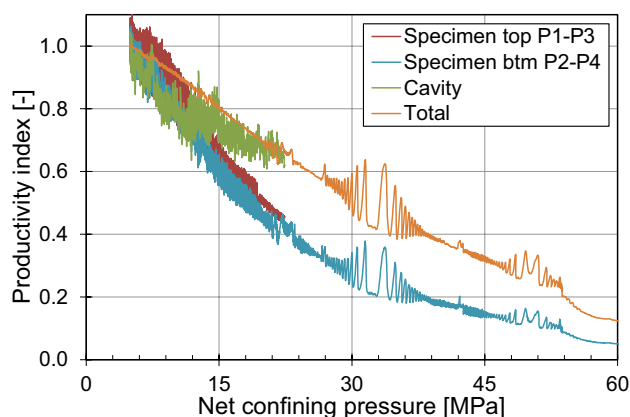

Fig. 27 PI evolution for 50% pack field core test between various measuring points

Fig. 28 PI evolution for 100% pack field core test between various measuring points

Table 2 Summary of the compaction test results

Sandstone		Castlegate			Saltwash South		
Test No		No. 1	No. 2	No. 3	No. 1	No. 2	No. 3
K_o	–	1/3	2/3	1	1/3	2/3	1
Porosity	%	28.0	27.5	27.5	31.2	31.6	31.8
Max σ'_{ax}	MPa	129.5	135.0	100.0	82.9	134.9	92.1
Max σ'_c	MPa	43.1	90.0	99.9	27.6	89.9	92.0
Grain crushing σ'_{ax}	MPa	128.3	–	–	79.7	120.4	–
Grain crushing σ'_c	MPa	42.8	–	–	26.6	80.3	–
Permeability	Darcy	0.91	0.91	0.75	3.04	2.09	1.87
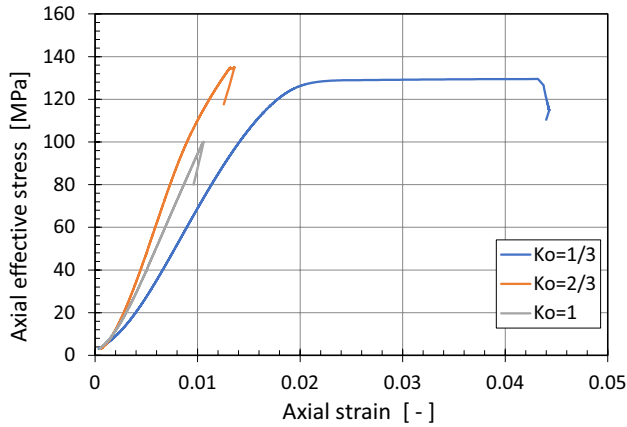
Fig. 29 Axial stress versus axial strain for all Castlegate compaction tests
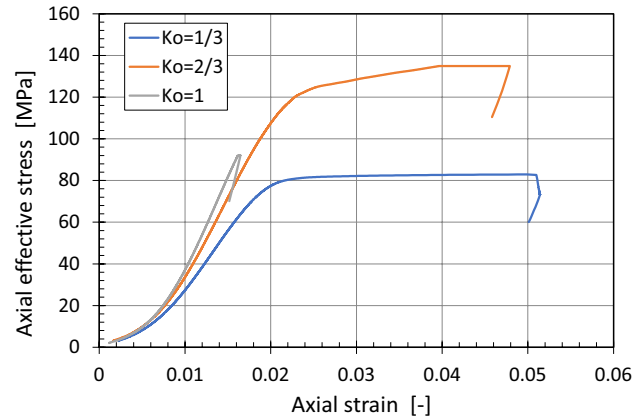
Fig. 31 Axial stress versus axial strain for all Saltwash South compaction tests
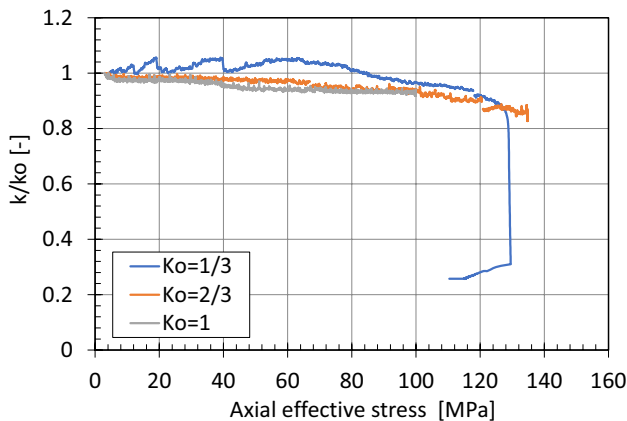
Fig. 30 Normalized axial permeability evolution during Castlegate compaction tests
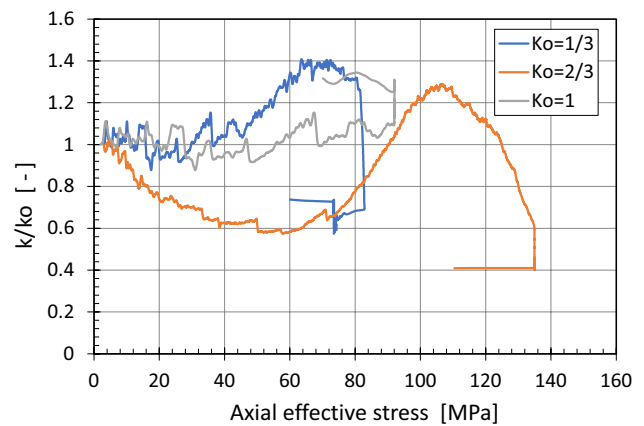
Fig. 32 Normalized axial permeability evolution during Saltwash South compaction tests

$K_0 = 1/3$, Saltwash South $K_0 = 1/3$ and 2/3), while the remainder were limited by equipment pressure capacity. Table 2 summarizes the tests.

The specimens that experienced grain crushing maintained the axial stress under large axial deformation.

Fig. 29 shows the axial effective stress versus axial strain for the three tests on Castlegate specimens, where only the test with $K_0 = 1/3$ experienced grain crushing. Axial permeability reduced rapidly at the grain crushing stress (Fig. 30). For $K_0 = 2/3$, the change of axial P and S-wave velocities with change in mean effective stress reached
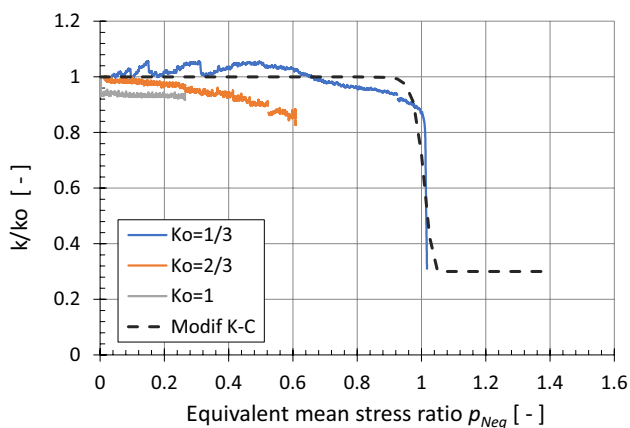
Fig. 33 Calibrated permeability loss model and experimental results for Castlegate

Fig. 34 Simulation of tangential strain for the Castlegate reference test compared with the experimental results

zero at the end of the test, indicating proximity to specimen yield. The corresponding values for $K_0 = 1$ were 0.5–1 m/(s·MPa), indicating that the specimen was not close to yielding.

For the tests on Saltwash South, both $K_0 = 1/3$ and $K_0 = 2/3$ showed grain crushing, with the latter increasing axial load capacity during compaction (Fig. 31). Permeability reduction (Fig. 32) was less rapid in the case of $K_0 = 2/3$ than $K_0 = 1/3$ since permeability is a function of strain rather than stress per se. The hydrostatic test with $K_0 = 1$ did not experience yield, and the ultrasonic velocities were strictly increasing during loading.

Permeability decrease due to compaction has been modelled extensively for various porous media. In the current work, we employ a modified Kozeny–Carman model which accounts for the sharp permeability decline during grain crushing or pore collapse, originally developed for the sudden pore collapse observed in high porosity chalks. The expression for the permeability is

$$k = k_0 \frac{1 - \phi_0^2}{\phi_0^3} \frac{\phi^3}{1 - \phi^2} \left[k_1 + \left(1 - k_1\right) e^{-k_2 p_{Neq}^{k_3}} \right] \quad (2)$$

where k_0 is a reference permeability, ϕ_0 reference porosity, ϕ is porosity, k_i are calibration parameters, and p_{Neq} is equivalent mean stress ratio defined by Eq. (3):

$$p_{Neq} = \frac{\sqrt{\langle p_N' - L_N \rangle^2 + R^2 \tau_N^2}}{1 - L_N} \quad (3)$$

See Sect. 4.6 for definition of the parameters. Figure 33 shows the calibrated permeability model and experimental results for Castlegate, using $k_1 = 0.3$, $k_2 = 0.5$, and $k_3 = 50$.
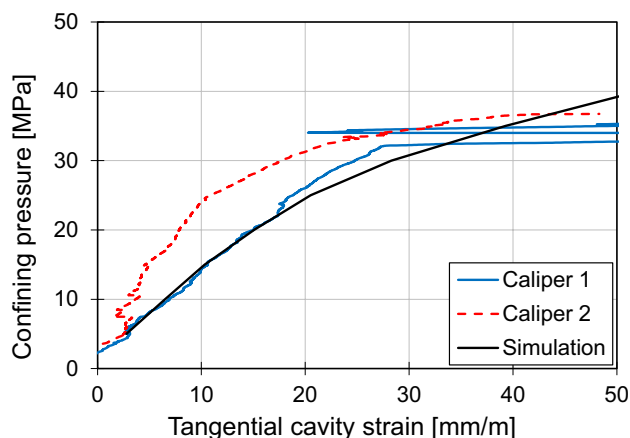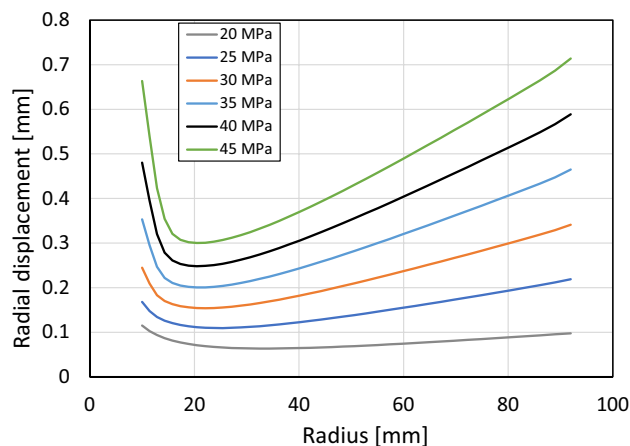

Fig. 35 Displacement versus radius for 0% packed Castlegate at increasing levels of confining stress
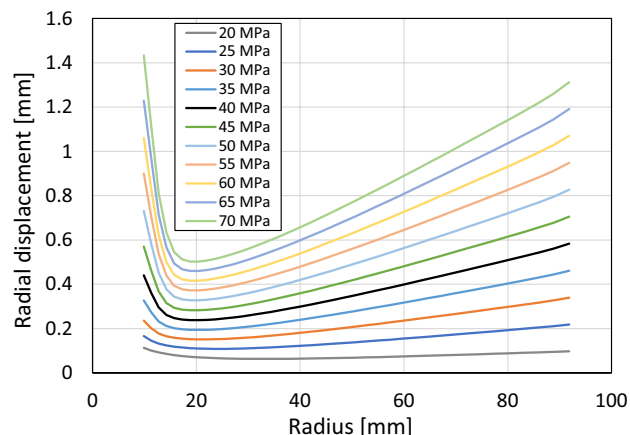

Fig. 36 Displacement versus radius for the upper, unsupported region of the 50% packed Castlegate at increasing levels of confining stress
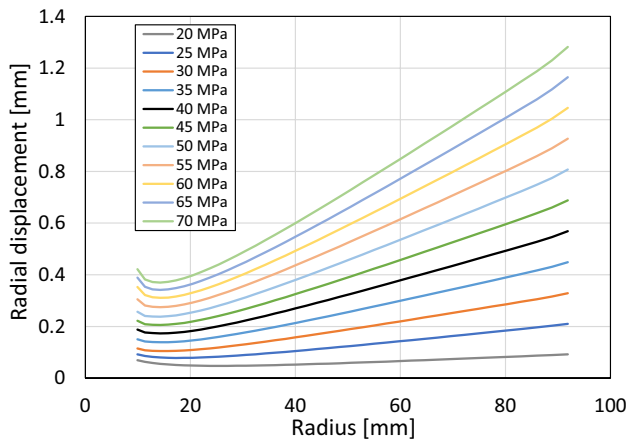
Fig. 37 Displacement versus radius for the lower, supported region of the 50% packed Castlegate at increasing levels of confining stress
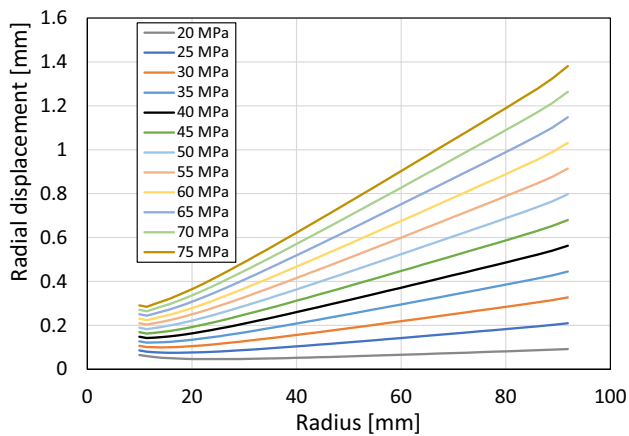

Fig. 38 Displacement versus radius for the 100% packed Castlegate at increasing levels of confining stress

Fig. 39 Displacement at the cavity wall versus confining stress for all simulations on Castlegate

Fig. 40 Displacement at the cavity wall versus confining pressure for the experimental and simulated cases of 0% packed and 50% packed Castlegate. For the simulations of 50% packing, the displacement is measured in the unsupported upper ("up") and supported lower ("lo") region

4.5 Numerical Simulations of Castlegate Perforation Productivity Decline Tests

As described in Section 3.2, yield parameters were chosen partially by matching tangential cavity strain in unsupported hollow cylinder loading experiments. Figure 34 shows the resulting match between simulated and experimentally measured tangential perforation strain.

Figures 35, 36, 37 and 38 plot radial displacement versus radius for various levels of confining pressure and proppant packing. In the unsupported and completely supported cases, the displacement is measured at the half height of the specimen, while for the partially supported case, displacement is measured at 75% height (half height of the unsupported region) and 25% height (half height of the supported region). In a purely elastic case, the tangential stress would increase, and radial stress decrease, towards the center. Within a
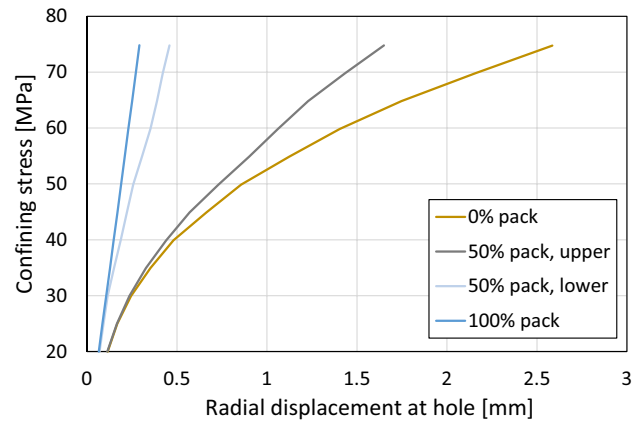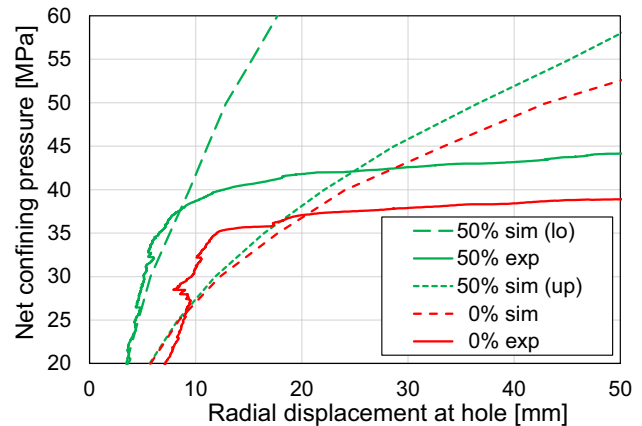
certain radius around the hole, the radial displacement starts to increase again due to elastic stress concentration and plastic rock dilation. The 50% packed perforation is seen to somewhat limit the perforation closure also in the upper, unsupported region (Fig. 36) as compared to the completely unsupported case (Fig. 35). At 45 MPa confining pressure, the deformations are 0.57 mm and 0.66 mm, respectively. The corresponding values for the lower, supported region of the 50% packed test (Fig. 37) and the completely supported perforation (Fig. 38) are 0.21 mm and 0.17 mm, respectively. Thus, under the assumptions made in the simulations, proppant packing severely limits perforation closure where the proppant is in direct contact with the perforation wall, but also limits deformation in adjacent areas. Figure 39 shows the radial displacement at the borehole wall versus confining pressure for all four cases described. A comparison with
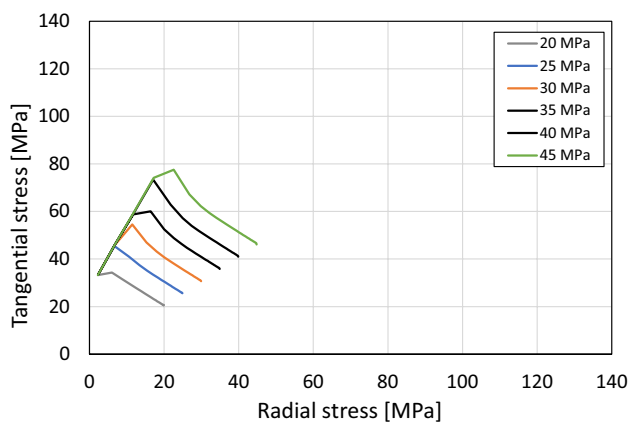
Fig. 41 Tangential versus radial stress along a radial trace for 0% packed Castlegate
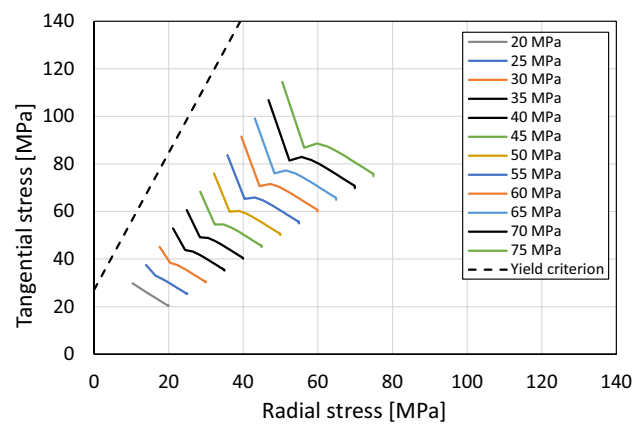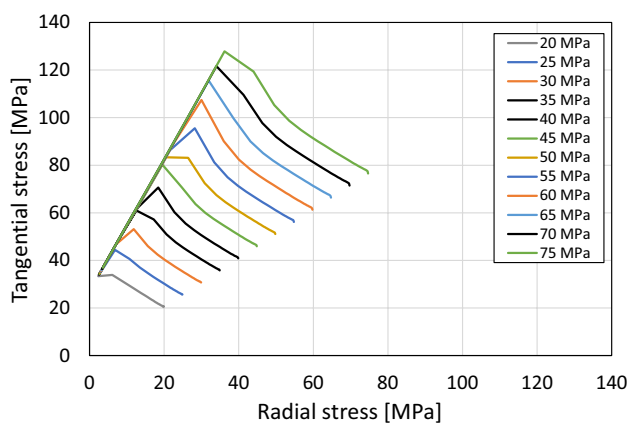

Fig. 42 Tangential versus radial stress along a radial trace for the upper, unsupported region of the 50% packed Castlegate
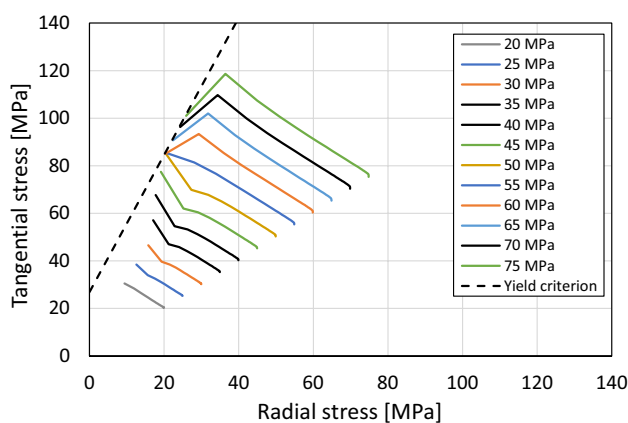

Fig. 43 Tangential versus radial stress along a radial trace for the lower, supported region of the 50% packed Castlegate. The yield criterion is indicated

Fig. 44 Tangential versus radial stress along a radial trace for the 100% packed Castlegate. The yield criterion is indicated

experimental results is shown in Fig. 40. The simulated displacements match very well until approximately 35 MPa, where the formation of breakouts cause large displacements in the experiments. For the 50% packing, the experimental measurements at the half-height of the specimen match the simulated measurements in the packed lower half considerably better than the unsupported upper half.

Figures 41, 42, 43 and 44 show the stress states in principal space for the four described cases. Each line represents a trace along the radius, plotting the tangential (maximum principal) versus radial (minimum principal) stress for each point along the trace. The stress is seen to be hydrostatic at the outer boundary, identical to the confining pressure. Radial stress decreases inward, while tangential stress increases towards the plastic radius, after which it follows the yield criterion. For unsupported regions (Figs. 41, 42), the cavity wall is expected to yield when the tangential stress reaches the unconfined compressive strength of the material (27 MPa), which occurs at approximately 13.5 MPa confining pressure. The plastic radius increases as expected for increasing levels of confining pressure. For the supported region in the 50% packed perforation (Fig. 43), yielding occurs only for higher levels of confining stress, while yielding does not occur at all for the completely supported perforation (Fig. 44).

4.6 Analysis of Perforation Yield

The grain crushing experiments are interpreted within a material model which includes a Mohr–Coulomb shear failure criterion, and an elliptical pressure cap intersecting the shear failure line (e.g. Chen and Mizuno 1990). The formulation of the pressure cap is
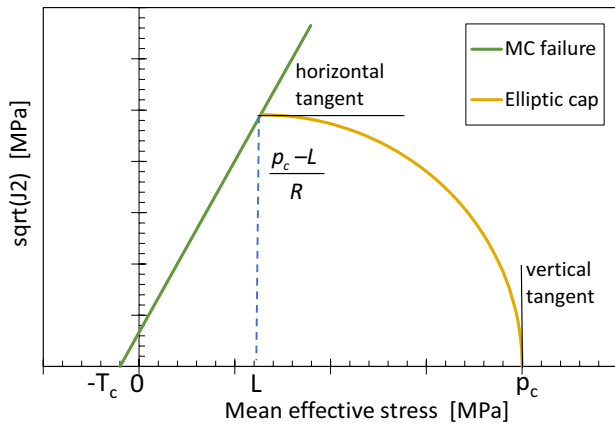
**Fig. 45** Representation of the grain crushing model with elliptical pressure cap

Table 3 Calibrated parameters for the combined Mohr–Coulomb and pressure cap model

| Sandstone		Saltwash South	Castlegate
L	MPa	40	64
p_c	MPa	125	200
L/p_c	–	0.32	0.32
R	–	2.77	2.77
T_c	MPa	1	10
φ	°	32	29

$$\frac{(p'-L)^2}{(p_c-L)^2} + \frac{R^2\tau^2}{(p_c-L)^2} = 1 \tag{4}$$

where p' is the mean effective stress, τ is the generalized shear stress ($\sqrt{J_2}$), p_c is the grain crushing hydrostatic stress, L is the center of the ellipse, and R is the major to minor ellipse axis ratio. Figure 45 shows the combined yield criterion.

The cap model parameters for Saltwash South were calibrated with the constraint of horizontal tangent at the Mohr–Coulomb shear failure line, and a best fit to the two experimental data points from the grain crushing tests. The values of L/p_c and R calibrated for Saltwash South were assumed to apply for Castlegate, and then L and p_c for Castlegate were found from a best fit to the single experimental data point. Table 3 shows the calibrated values for both rocks. Wong et al. (1997) studied brittle failure and shear-enhanced compaction in several sandstones and found that most compaction failures were bounded by the elliptical caps defined by $L/p_c = 0.5$ and $1.24 < R < 1.73$, indicating that in the current experiments, the transition from shear to compaction failure happened at a lower value of normalized shear stress.
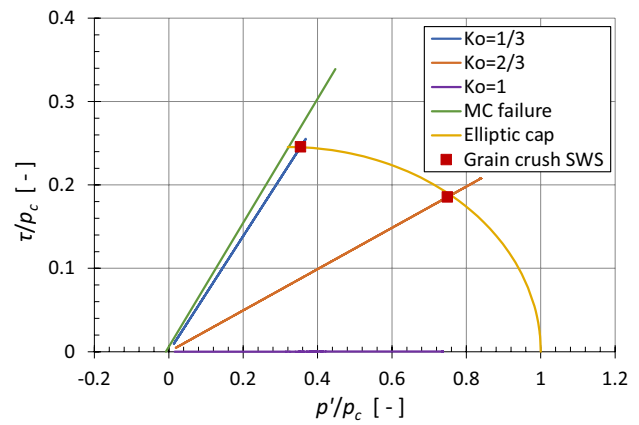
(a)
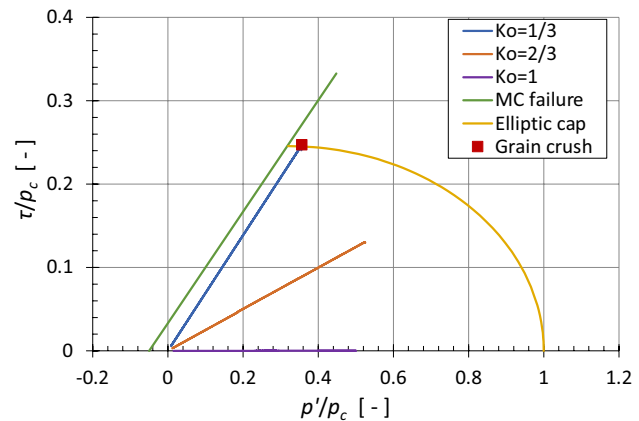
(b)

Fig. 46 Calibrated shear and pressure cap model plotted in normalized stress space for **a** Saltwash South and **b** Castlegate. Grain crushing tests are shown; note the hydrostatic test along the horizontal axis
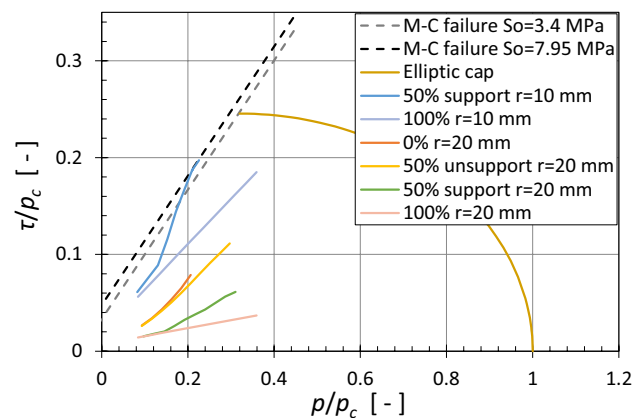

Fig. 47 Simulated stress paths for points at the borehole wall ($r = 10$ mm) and slightly inside the material ($r = 20$ mm) for Castlegate specimens. Two Mohr–Coulomb failure lines are shown: one using cohesion based on the triaxial tests (3.4 MPa cohesion), and the other, used in the simulations, using the cohesion calibrated from hollow cylinder tests (7.95 MPa)

The calibrated cap models for Saltwash South and Castlegate are shown in Fig. 46, where both shear stress and mean stress are normalized by the grain crushing hydrostatic stress p_c. The stress paths for the grain crushing tests and resulting grain crushing stress (Table 2) are shown in Fig. 46. The simulated stress paths over time (increasing confining pressure) at various points in the hollow cylinder specimen close to the cavity wall are plotted in Fig. 47. The stress state at the cavity wall ($r = 10$ mm) for the completely unsupported (0%) and unsupported region of the partially supported (50%) cavity quickly reached shear failure and are omitted from the figure. Under the stated assumption in the simulations that material is not eroded and exhibits perfect plasticity, stress states within ($r = 20$ mm) the rock are far away from yield, especially supported regions due to the decreased stress concentration and thus decreased shear stress. For unsupported regions, this is clearly in disagreement with observed failure patterns (Figs. 13, 18), and a softening model would likely lead to more accurate results for these cases of little to no lateral confinement. The purpose of the simulations, though, is to analyze the stress states for supported cavities where the material is kinematically constrained, which may call for higher post-peak load bearing capacity of the material. The stress states closest to yielding are the ones on the supported cavity walls. The small amount of support increases mean stress and move the stress states mostly parallel to the shear failure line, approaching the pressure cap.

Note that the Mohr–Coulomb shear failure criterion is defined in terms of generalized shear stress and mean stress where a conventional triaxial stress state is assumed, so that the intermediate principal stress is equal to the minor principal stress, i.e., $p_{TRX} = (\sigma_1 + 2\sigma_3)/3$. The actual mean stress in the hollow cylinder is close to $p_{HC} = \sigma_C$ in the elastic region and will for material undergoing plastic yielding be slightly lower, but it will nevertheless be larger than the triaxial mean stress since $\sigma_2 > \sigma_3$. A conventional triaxial mean stress is used to plot the stress paths consistent with the shear failure line, although the true mean stress is somewhat higher. The hollow cylinder normalized mean stress at the end of the simulations were approximately 10–20% higher than plotted.

5 Discussion

The constitutive equations for the experimentally tested and simulated materials deserve some discussions. Castlegate sandstone was modelled with perfect plasticity, which may be appropriate under considerable confinement, and when clear discontinuities are not produced. Both in low-confinement compression tests and in unsupported hollow cylinder compression tests, the load-bearing capacity is seen to reduce post-peak. This is evident in, e.g., the calibration

of internal cavity strain shown in Fig. 34. Initial straining is matched appropriately by the simulations, but the lack of softening underestimates the strain at increasing loads. It was assumed, however, that proppant support would contribute to less softening of the rock material, and for simplicity, perfect plasticity was used. The simulations indicate that the yielding of the partially supported cavity wall happens at quite high radial stress (Fig. 43), so that modelling the material with some load bearing capacity post-yield seems appropriate.

The resulting increase of radial stress at the cavity wall is dependent on the support from the proppant. As mentioned in Sect. 3.2, the proppant was modelled with non-negligible cohesion, which may be a strong assumption for this material, and should be considered an upper bound of the load bearing capacity of loosely packed proppant without a rigid boundary vertically. The productivity decline in unsupported cavities in the current experiments on outcrop rock specimens is clearly due to clogging of the very limited area representing the perforation through the casing. The possible causes of productivity decline of the supported outcrop cavities are proppant-formation interface permeability reduction, failure of the cavity wall in either shear or shear-induced compaction without subsequent erosion, and filtering and clogging of the proppant pack by fines and/or produced sand. Numerical simulations indicate that the partially supported cavity yields in shear and that the fully supported cavity does not yield at all (Fig. 47), although the fully supported cavity also experiences productivity decline. Apart from fines production, and if the proppant support in the current simulations is indeed an upper bound, it is more likely that the stress state at the cavity wall is close to or at the shear line than the pressure cap, and grain crushing as observed in the compaction experiments seem unlikely in the hollow cylinder experiments.

Simulations predict radial stress at the interface for the partially supported cavity at 20–30 MPa (Fig. 43), and as much as 50 MPa at the end of the test for the fully supported cavity (Fig. 44). Crawford et al. (2018) studied flow perpendicular to propped fractures in moderately low permeability formations (20–40 mD) and found that the proppant-formation interface permeability was roughly two orders of magnitude lower than that of the formation, with very little change over the initial 50 MPa closure stress. The damaged zone thickness was assumed to correspond to the closure of the fracture (0.1–0.2 mm at 20 MPa), but if the thickness is rather defined as the region of observed grain cracking (1–2 mm), the permeability reduction is approximately one order of magnitude relative to the formation. Closure (and average permeability reduction) was greatest during the initial ~ 20 MPa stress increase, and this may indicate the stress range over which proppant embedment is most

significant. Reinicke et al. (2013) did similar experiments on Bentheim sandstone while monitoring acoustic events with p-wave transducers. They observed a permeability reduction of the interface of almost 88% at 21 MPa differential stress (fracture perpendicular stress minus fracture parallel stress), and over 80% reduction at only 2 MPa closure stress. The damaged zone thickness was estimated at 4 mm from acoustic events, but significant damage was evident at 21 MPa differential stress and beyond. Given that Bentheim is significantly stronger than Castlegate at approximately 45 MPa UCS (Reinicke 2011), and that the formation at greater depths than 9200 m reported by Crawford et al. (2018) also likely is stronger, we assume that Castlegate would experience similar interface permeability reduction at equal or lower normal stress.

A permeability reduction of this order (90%) in the interface of a hydraulic fracture of 60 m half width contributes to a reduction of well productivity of the order of 0.1% (Reinicke et al. 2013) and is therefore of little practical concern, although such a reduction could have much greater effects on perforations of significantly smaller interfacial area, as the current experiments also suggest. Although the permeability reduction under grain crushing is quite abrupt in an element test (Fig. 33), it would manifest itself more gradually around a progressively yielding cavity. Interface damage by proppant embedment also seems to progress gradually. Using a simplified version of the modified Kozeny–Carman permeability equation (Eq. (2)), where the permeability is a step function, so that $k = k_0$ for $p < p_c$, and else $k = k_1$, we can analytically estimate the resulting permeability, or productivity, of a yielding cavity, and employ the same model for interface damage. The expression for the normalized permeability is

$$\frac{k}{k_0} = \frac{\ln\left(\frac{r_e}{r_i}\right)}{\frac{1}{k_1}\ln\left(\frac{r_y}{r_i}\right) + \ln\left(\frac{r_e}{r_y}\right)} \tag{5}$$

where r_e and r_i are the external and internal radii respectively and r_y is the yield radius. Figure 48 shows the normalized effective permeability of a hollow cylinder as a function of yield radius, under the assumption of the simplified permeability model for the values k_1 found in the current grain crushing tests ($k_1 = 0.3$) and reported in the literature for the interface damaged zone ($k_1 = 0.1$). A productivity reduction of 40% as seen at the end of the 100% supported perforation (Fig. 26) is predicted at a yield radius of 19 mm (9 mm into the rock) for pressure compaction, and only 11.75 mm (1.75 mm into the rock) for proppant embedment damage. A pressure yield radius of 19 mm is not supported by the simulated stress paths, which show that the stress 10 mm into the rock is far away from yielding for supported cavities (Fig. 47). More likely mechanisms for productivity decline are proppant-formation interface damage or cavity wall shear damage and proppant clogging.

6 Conclusions

Productivity decline experiments were run on hollow cylinder specimens from two sets of outcrop sandstone and one set of unconsolidated field core, with varying degrees of proppant packing. Completely unsupported perforations in outcrop specimens yielded and produced sand according to their sandstone class. The productivity around the perforation increased due to erosion of the cavity wall and an increase of inflow area, but the total productivity of the system decreased significantly when produced sand was filtered through the narrow proppant-filled casing perforation. Thus, poorly packed perforations may cause significant productivity decline if the filtrating proppant bed area is small. The unsupported perforation in unconsolidated field core collapsed at low confining pressure and before any fluid flow was measured. The resulting productivity of the system was two orders of magnitude lower than for partially and fully supported perforations.

Incomplete packing of perforations may not be detrimental to perforation productivity if the proppant pack spans the diameter of the cavity, and thus is able to provide radial support and a highly permeable flow channel. In most perforation orientations, a partial proppant pack will likely not be as advantageous as in the current experiments with vertical perforations, and the current results for partial packing are likely best-case scenarios since a
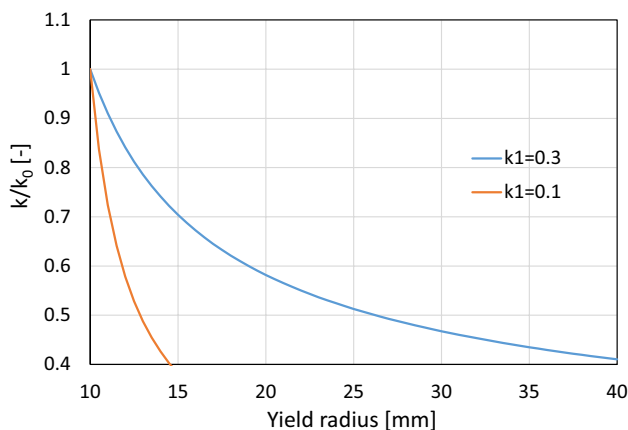
Fig. 48 Normalized effective permeability of a hollow cylinder as a function of yield radius

permeable flow channel is maintained close to the casing perforation entrance.

Partial packing likely delays productivity decline by a combination of mechanical support and hydraulic conductivity. Complete packing supports the perforated cavities well but possibly introduces other mechanisms of productivity decline close to or at the formation-proppant interface. Experimental grain crushing tests on the tested rock material combined with numerical simulations of the hollow cylinder tests indicate that formation permeability reduction by grain crushing due to high mean stress is unlikely to be a cause of productivity decline. Proppant-formation interface damage as reported in the literature occurs at interface normal stresses predicted in the current simulations and are a possible productivity decline mechanism in our experiments along with produced sand filtering.

Author Contributions EP is project manager, proposed the main idea of the experiments, analyzed compaction experiments and devised permeability model. ANB designed and conducted experiments, analyzed data, and wrote manuscript draft. XX set up numerical model, performed simulations, and assisted to format manuscript. GL provided field core material. GL and ZY contributed with field relevance in experimental design and results discussion.

Data availability The participants of this study did not give written consent for their data to be shared publicly, so due to the nature of some of the data supplied, the research supporting data is not available.

Declarations

Conflict of Interest The authors have no competing interests.

References

Anderson RW, Cooke CE Jr, Wendorff CL (1989) Propping agents and fracture conductivity. Recent Adv Hydraul Fract 12:109–130

Bellarby J (2009) Well completion design, 1st edn. Elsevier, Amsterdam

Berntsen AN, Papamichos E (2012) Scale effect in volumetric sand production. In: Paper presented at the 46th U.S. Rock Mechanics/Geomechanics Symposium, Chicago, Illinois, June 2012. ARMA-2012–482.

Chen W-F, Mizuno E (1990) Nonlinear analysis in soil mechanics. Elsevier, Amsterdam

Crawford BR, Homburg JM, Freysteinson JA, et al (2018) Evaluating mechanical damage and closure stress effects on hydraulic fracture treatments using novel geomechanics laboratory testing: application to Julia Field, Gulf of Mexico. In: Paper presented at the 52nd U.S. Rock Mechanics/Geomechanics Symposium, Seattle, Washington, June 2018. ARMA-2018–430

Fjær E, Holt RM, Raaen A et al (2008) Petroleum related rock mechanics, 2nd edn. Elsevier, Amsterdam

Fjær E, Horsrud P, Bautmans P (2017) Scaling issues in hollow cylinder tests on shale. In: Paper presented at the 51st U.S. Rock Mechanics/Geomechanics Symposium, San Francisco, California, USA, June 2017

Han Y, Tallin AG, Wong GK (2015) Impact of depletion on integrity of sand screen in depleted unconsolidated sandstone formation. In: Paper presented at the 49th U.S. Rock Mechanics/Geomechanics Symposium, San Francisco, California, June 2015. ARMA-2015–301

Homburg JM, Crawford BR, Reese WC, et al (2018) Evaluating the mechanism of mechanical damage and stress effects on fracture treatments using textural and chemical characterization: application to Julia Field, GOM. In: Paper presented at the 52nd U.S. Rock Mechanics/Geomechanics Symposium, Seattle, Washington, June 2018. ARMA-2018–572

Itasca (2020) FLAC3D, Fast Lagrangian Analysis of Continua. Version 7.0. Itasca Consulting Group, Minneapolis, Minnesota

Papamichos E (2010) Analysis of borehole failure modes and pore pressure effects. Comput Geotech 37:141–152. https://doi.org/10.1016/j.compgeo.2009.08.006

Papamichos E, Tronvoll J, Skjærstein A, Unander TE (2010) Hole stability of Red Wildmoor sandstone under anisotropic stresses and sand production criterion. J Petrol Sci Eng 72:78–92. https://doi.org/10.1016/j.petrol.2010.03.006

Papamichos E, Stenebraten J, Cerasi P, et al (2008) Rock type and hole failure pattern effects on sand production. In: Paper presented at the The 42nd U.S. Rock Mechanics Symposium (USRMS), San Francisco, California, June 2008. Paper ARMA-08–217

Reinicke A (2011) Mechanical and hydraulic aspects of rock-proppant systems: laboratory experiments and modelling approaches. Dissertation. Universität Potsdam

Reinicke A, Blöcher G, Zimmermann G, Huenges E, Dresen G, Stanchits S, Legarth B, Makurat A (2013) Mechanically induced fracture-face skin—insights from laboratory testing and modeling approaches. SPE Prod Oper 28:26–35. https://doi.org/10.2118/144173-PA

Sulem J, Vardoulakis I, Papamichos E et al (1999) Elasto-plastic modelling of Red Wildmoor sandstone. Mech Cohesive-Frict Mater 4:215–245. https://doi.org/10.1002/(SICI)1099-1484(199905)4:3%3c215::AID-CFM61%3e3.0.CO;2-8

Wong T, David C, Zhu W (1997) The transition from brittle faulting to cataclastic flow in porous sandstones: mechanical deformation. J Geophys Res Solid Earth 102:3009–3025. https://doi.org/10.1029/96JB03281

Zhao XG, Kai C (2010) A mobilized dilation angle model for rocks. Int J Rock Mech Min Sci 47:368–384. https://doi.org/10.1016/j.ijrmms.2009.12.007

Publisher's Note Springer Nature remains neutral with regard to jurisdictional claims in published maps and institutional affiliations.